Geoscientific
Model Development
Discussions

Open Access

Objectified quantification of uncertainties in Bayesian atmospheric inversions

A. Berchet, I. Pison, F. Chevallier, P. Bousquet, J.-L. Bonne, and J.-D. Paris

Laboratoire des Sciences du Climat et de l'Environnement, CEA-CNRS-UVSQ, IPSL, Gif-sur-Yvette, France

GMDD

7, 4777–4827, 2014

Objectified uncertainty quantification

A. Berchet et al.

Title Page

Abstract	Introduction
Conclusions	References
Tables	Figures

|◄ ►|

◄ ►

Back Close

Full Screen / Esc

Printer-friendly Version

Interactive Discussion

Abstract

Classical Bayesian atmospheric inversions process atmospheric observations and prior emissions, the two being connected by an observation operator picturing mainly the atmospheric transport. These inversions rely on prescribed errors in the observations, the prior emissions and the observation operator. At the meso-scale, inversion results are very sensitive to the prescribed error distributions, which are not accurately known. The classical Bayesian framework experiences difficulties in quantifying the impact of mis-specified error distributions on the optimized fluxes. In order to cope with this issue, we rely on recent research results and enhance the classical Bayesian inversion framework through a marginalization on all the plausible errors that can be prescribed in the system. The marginalization consists in computing inversions for all possible error distributions weighted by the probability of occurence of the error distributions. The posterior distribution of the fluxes calculated by the marginalization is complicated and not explicitly describable. We then carry out a Monte-Carlo sampling relying on an approximation of the probability of occurence of the error distributions. This approximation is deduced from the well-tested algorithm of the Maximum of Likelihood. Thus, the marginalized inversion relies on an automatic objectified diagnosis of the error statistics, without any prior knowledge about the matrices. It robustly includes the uncertainties on the error distributions, contrary to what is classically done with frozen expert-knowledge error statistics. Some expert knowledge is still used in the method for the choice of emission aggregation pattern and sampling protocol in order to reduce the computation costs of the method. The relevance and the robustness of the method is tested on a case study: the inversion of methane surface fluxes at the meso-scale with real observation sites in Eurasia. Observing System Simulation Experiments are carried out with different transport patterns, flux distributions and total prior amounts of emitted gas. The method proves to consistently reproduce the known "truth" in most cases, with satisfactory tolerance intervals. Additionnaly, the method explicitly provides influence scores and posterior correlation matrices. An in-depth interpretation

of the inversion results is then possible. The more objective quantification of the influence of the observations on the fluxes proposed here allows us to evaluate the impact of the observation network on the characterization of the surface fluxes. The explicit correlations between emission regions reveal the mis-separated regions, hence the typical temporal and spatial scales the inversion can analyze. These scales proved to be consistent with the chosen aggregation patterns.

1   Introduction

Characterizing the global biogeochemical cycles of greenhouse gases requires reliably understanding the exchanges at the surface-atmosphere interface. The description of these exchanges must encompass the absolute amounts of gas released to and removed from the atmosphere at the surface interface, the spatial distribution and the temporal variability of the fluxes, and the determination of the underlying physical processes of emissions and sinks. Such an integral depiction is still missing for most greenhouse gases (Ciais et al., 2013). One of the possible approaches to inquire into the surface fluxes is the analysis of the atmospheric signal. The drivers of the spatial and temporal variability of the atmospheric composition are the transport, the atmospheric chemistry and the surface fluxes (e.g., Seinfeld J. H. and Pandis S. N., 2006). Therefore, monitoring the atmospheric composition and using a representation of the atmospheric transport and chemistry with Global Circulation Models (GCMs) or Chemistry-Transport Models (CTMs) can help in inferring back information on the fluxes (Bousquet et al., 2006; Bergamaschi et al., 2010). This approach, called atmospheric inversion, suffers two practical issues in its implementation. First, the atmospheric composition is still laconically documented, though the number of global monitoring projects with extensive surface observation networks and satellite platforms has been increasing for more than two decades (e.g., Dlugokencky et al., 1994, 2009). Indeed, the satellite platforms have a global coverage but the observed atmospheric composition is integrated on the vertical column, while the surface sites can provide continuous

Objectified uncertainty quantification

A. Berchet et al.

observations but at fixed point locations. Second, the atmosphere behaves as an integrator and the air masses are mixed ambivalently through the transport (Enting et al., 1993). Thus, the inverse problem of tracking back the fluxes from the variability of the atmospheric composition cannot be solved deterministically. The Bayesian formalism makes statistical analyses of the atmospheric signal possible in order to identify confidence intervals of fluxes compatible with the atmospheric composition (Tarantola, 1987).

Bayesian inversions have been extensively used at the global scale, providing insights on the greenhouse gas budgets (e.g., Gurney et al., 2002; Kirschke et al., 2013; Bergamaschi et al., 2013). However, non compatible discrepancies appear between the possible configurations of atmospheric inversion systems (Peylin et al., 2013). The various configurations include the choice of the atmospheric transport, its spatial and temporal resolutions, the meteorological driving fields, the type and density of the observations, etc. In the Bayesian formalism, some assumptions also have to be made on the statistics of the errors the transport model makes, on the errors made when comparing a discretized model to observations (Geels et al., 2007) and on the confidence we have on the prior maps and time profiles of emissions (Enting, 2002). All these choices are based on technical considerations and on the expert perception of the problem to solve. Comparing results based on different choices that are physically adequate, but subjective, is difficult, especially to track inconsistencies, which enlarge the range of flux estimates.

In the following, we focus on the developement of an enhanced Bayesian method that objectifies the assumptions on the statistics of the errors and that takes into account the unavoidable uncertainties generated by our lack of knowledge on these error statistics. The confidence ranges of the inverted surface fluxes are computed by a Monte-Carlo marginalization on the possible error statistics. The weight function for the marginalization is inferred from an already-tested Maximum of Likelihood approach (Michalak et al., 2005), processing the pieces of information carried by the differences between the measurements and the prior simulated concentrations. The potential and

consistency of the method is tested through Observing System Simulation Experiments (OSSEs) on a realistic configuration of atmospheric inversion. The case study is the quantification of methane fluxes in the Siberian Lowlands with a network of surface observation sites that have been operated for a few years by the Japanese National In-
⁵ stitute for Environmental Studies (Sasakawa et al., 2010) and the German Max Planck Institute (Winderlich et al., 2010). The characterization of the region is challenging, with co-located massive methane emissions from anthropogenic activity (oil and gas extraction) and from wetlands in summer. Moreover, the wetland emissions have a very high temporal variability (due to their sensitivity to the water table depth and to the tempera-
¹⁰ ture; e.g., Macdonald et al., 1998; Hargreaves and Fowler, 1998). Their quantification is then difficult. In order to catch the influence of the sampling bias due to non-regularly distributed observation sites and non-continuous measurements, we produce virtual observations from a known "truth" at locations where real observations are carried out and at dates when the logistical issues do not prevent the acquisition of measurements.
¹⁵ We then check the capability of our method to reproduce consistent flux variability and distribution with 7 degraded inversion configurations (perturbed transport, flat flux distributions, etc.).

In Sect. 2, we describe the theoretical framework of our method of marginalization. The enhancements on the general theoretical framework need a cautious definition of
²⁰ the problem to be implementable in term of computational costs and memory limits. In Sect. 3, guidelines for a suitable definition of the problem are developed. The whole structure of the method is summarized in Sect. 4.1. In Sect. 4, we present the particular set up of the OSSE carried out for proving the robustness of the method. The specific Siberian configuration we test our method on is detailed in Sect. 5. The OSSE are
²⁵ evaluated along defined objective statistical scores in Sect. 6.

2   Marginalized Bayesian inversion

In statistics, marginalizing a probability density function (pdf) $p(\boldsymbol{x})$ consists in rewriting it as a sum of conditional probabilities $p(\boldsymbol{x}|\boldsymbol{z})$ weighted by $p(\boldsymbol{z})$. Most atmospheric inversions do not rely on a marginalization over the possible prior and observation error covariance matrices: they select just one of each, either because they do not have any information about the uncertainty of these matrices or because they cannot technically exploit such information. We first describe the motivations for using a marginalized inversion in Sect. 2.1. In Sect. 2.2, we describe the Monte-Carlo approach chosen in order to compute the marginalization.

2.1   Motivations and outlines

The surface-atmosphere fluxes, through transport, cause a variability in the atmospheric mixing ratios of the species we are interested in. The atmospheric inversion relies on the processing of the atmospheric varibility in order to infer back the surface-atmosphere fluxes. Since the atmosphere is diffusive and mixes irreversibly air masses from different origins, it is physically impossible to infer deterministic information on the fluxes from the integrated atmospheric signal alone (Tarantola, 1987; Enting, 2002). We are then pursuing a thorough characterization of the pdf of the state of the system (i.e. the spatial and temporal distribution of the surface fluxes), assuming some prior knowledge on the system and having some observations of the atmospheric physical variables related to our problem. That is to say, we want to calculate the pdf $p(\boldsymbol{x}|\boldsymbol{y}^0 - H(\boldsymbol{x}^b), \boldsymbol{x}^b)$ for all possible states $\boldsymbol{x}$; $\boldsymbol{y}^0$ is a vector gathering all the available observations, $\boldsymbol{x}^b$ is the background vector including the prior knowledge on the state of the system and H is the observation operator converting the information in the state vector to the observation space. Typically, H embraces the atmospheric transport and the discretization of the physical problem. In the scope of applications of the atmospheric inversions, the observation vector $\boldsymbol{y}^0$ gathers measurements of dry air mole fraction. As for the observation operator, it is computed with a model which simulates

Title Page

Abstract | Introduction

Conclusions | References

Tables | Figures

◄ | ►►

◄ | ►

Back | Close

Full Screen / Esc

Printer-friendly Version

Interactive Discussion

mixing ratios. As we are interested in trace gases, we will consider that the dry air mole fractions can be assimilated to mixing ratios. In all the following, we also consider that H is linear; hence, H is assimilated to its Jacobian matrix $\mathbf{H}$ and $H(\mathbf{x}^b) = \mathbf{H}\mathbf{x}^b$. This approximation is valid for all non reactive atmospheric species at a scale large enough

5   for the turbulence to be negligible. When the atmospheric chemistry must be taken into account (for instance with methane), either the window of inversion must be short compared with the typical lifetime in the atmosphere for the linear assumption to be valid, or the concentration fields of the reactant species (e.g., OH radicals for methane) must be known.

10   In general, the characterization of the pdf is built within the Bayesian formalism with the assumption that all the involved pdfs are normal distributions (Enting et al., 1993). The pdfs are then explicitly described through their node and their matrix of covariance. In this case, the pdf $p(\mathbf{x}|\mathbf{y}^0 - \mathbf{H}\mathbf{x}^b, \mathbf{x}^b) \propto \mathcal{N}(\mathbf{x}^a, \mathbf{P}^a)$ is defined by its node, $\mathbf{x}^a$, the posterior state and its matrix of covariance, $\mathbf{P}^a$. In addition to the linear assumption, we

15   also consider that the uncertainties are unbiased. That is to say: $p(\mathbf{x} - \mathbf{x}^b) \propto \mathcal{N}(\mathbf{0}, \mathbf{B})$ and $p(\mathbf{y}^0 - \mathbf{H}\mathbf{x}^t) \propto \mathcal{N}(\mathbf{0}, \mathbf{R})$ where $\mathbf{x}^t$ is the true state of the system. In this context, we define the uncertainty matrices $\mathbf{B}$ and $\mathbf{R}$. $\mathbf{B}$ (resp. $\mathbf{R}$) encompasses the uncertainties on the background $\mathbf{x}^b$ (resp. on the measurements and on the model). Under these assumptions, we can explicitly write the posterior vector and the posterior matrix of

20   covariance: $\mathbf{x}^a = \mathbf{x}^b + \mathbf{K}(\mathbf{y}^0 - \mathbf{H}\mathbf{x}^b)$ and $\mathbf{P}^a = \mathbf{B} - \mathbf{K}\mathbf{H}\mathbf{B}$, with $\mathbf{K} = \mathbf{B}\mathbf{H}^T(\mathbf{R} + \mathbf{H}\mathbf{B}\mathbf{H}^T)^{-1}$ the Kalmam gain matrix.

The atmospheric inversion is straightforward (apart from technical issues in the implementation of the theory on computers) as long as these uncertainty matrices are defined. Indeed, some of these errors can be calculated unambiguously, such as mea-

25   surement errors. Other errors are derived, in most cases, following expert knowledge on, e.g., the behaviour of the atmospheric transport and of the surface fluxes. This expert knowledge is acquired, for example, through extensive studies on the sensitivity of the transport model to its parameterization and forcing inputs (e.g., Denning et al., 1999; Ahmadov et al., 2007; Lauvaux et al., 2009; Locatelli et al., 2013), or by

comparing prior fluxes to measured local fluxes (e.g., Chevallier et al., 2006). Some studies also rely on purely physical considerations (e.g., Bergamaschi et al., 2005, 2010). But the complex and unpredictible structure of the uncertainties is hard to reproduce accurately from the expert knowledge alone and an ill-designed tuple of uncertainty matrices $(\mathbf{R}, \mathbf{B})$ can have a dramatic impact on the inversion results (e.g., Berchet et al., 2013; Cressot et al., 2014). The discrepancies between the possible configurations of inversion can reveal some biases in the models: $p(\mathbf{y}^0 - \mathbf{H}\mathbf{x}^\text{t}) \propto \mathcal{N}(\boldsymbol{\eta}, \mathbf{R})$ instead of $p(\mathbf{y}^0 - \mathbf{H}\mathbf{x}^\text{t}) \propto \mathcal{N}(\mathbf{0}, \mathbf{R})$. For example, the horizontal wind fields can be biased or the vertical mixing in the planetary boundary layer systematically erroneous. That makes it difficult to compare simulated concentrations in the boundary layer to measurements (e.g., Peylin et al., 2002; Dee, 2005; Geels et al., 2007; Williams et al., 2013; Lauvaux and Davis, 2014). For our study, we neglect the biases in the inversion. We then focus only on the mis-specification of the uncertainty matrices $\mathbf{R}$ and $\mathbf{B}$.

In order to account for the uncertainties in the characterization of the uncertainties, we compute the pdf $p(\mathbf{x}|\mathbf{y}^0 - \mathbf{H}\mathbf{x}^\text{b}, \mathbf{x}^\text{b})$ by a marginalization on the uncertainty matrices.

2.2 Monte-Carlo marginalization

In the marginalization framework, the complete pdf $p(\mathbf{x}|\mathbf{y}^0 - \mathbf{H}\mathbf{x}^\text{b}, \mathbf{x}^\text{b})$ is separated into a sum of the contribution of each possible tuple of covariance matrices $(\mathbf{R}, \mathbf{B})$ weighted by the probability of occurence of the said tuple $(\mathbf{R}, \mathbf{B})$:

$$
\begin{aligned}
p(\mathbf{x}|\mathbf{y}^0 - \mathbf{H}\mathbf{x}^\text{b}, \mathbf{x}^\text{b}) &= \int_{(\mathbf{R}, \mathbf{B})} p(\mathbf{x}|\mathbf{y}^0 - \mathbf{H}\mathbf{x}^\text{b}, \mathbf{x}^\text{b}, \mathbf{R}, \mathbf{B}) \cdot p(\mathbf{R}, \mathbf{B}|\mathbf{y}^0 - \mathbf{H}\mathbf{x}^\text{b}, \mathbf{x}^\text{b}) \mathrm{d}(\mathbf{R}, \mathbf{B}) \\
&\propto \int_{(\mathbf{R}, \mathbf{B})} \mathcal{N}(\widetilde{\mathbf{x}^\text{a}}, \widetilde{\mathbf{P}^\text{a}}) \cdot p(\mathbf{R}, \mathbf{B}|\mathbf{y}^0 - \mathbf{H}\mathbf{x}^\text{b}, \mathbf{x}^\text{b}) \mathrm{d}(\mathbf{R}, \mathbf{B})
\end{aligned}
\tag{1}
$$

In Eq. (1), $\widetilde{(.)}$ depicts a local dependence to $(\mathbf{R}, \mathbf{B})$. This general expression encompasses the classical case with only one tuple of matrices $(\mathbf{R}, \mathbf{B})$ which considers $p(\mathbf{R}, \mathbf{B}|\mathbf{y}^0 - \mathbf{H}\mathbf{x}^\text{b}, \mathbf{x}^\text{b})$ as a Dirac-like distribution. More generally, $p(\mathbf{R}, \mathbf{B}|\mathbf{y}^0 - \mathbf{H}\mathbf{x}^\text{b}, \mathbf{x}^\text{b})$ is

not so well known. Using Bayes' rule, $p(\mathbf{R}, \mathbf{B}|\mathbf{y}^0 - \mathbf{H}\mathbf{x}^b, \mathbf{x}^b)$ can be re-written as:

$$p(\mathbf{R}, \mathbf{B}|\mathbf{y}^0 - \mathbf{H}\mathbf{x}^b, \mathbf{x}^b) = \frac{p(\mathbf{y}^0 - \mathbf{H}\mathbf{x}^b|\mathbf{R}, \mathbf{B}, \mathbf{x}^b) \cdot p(\mathbf{R}, \mathbf{B}|\mathbf{x}^b)}{\displaystyle\int_{(\mathbf{R},\mathbf{B})} p(\mathbf{y}^0 - \mathbf{H}\mathbf{x}^b|\mathbf{R}, \mathbf{B}, \mathbf{x}^b) \cdot p(\mathbf{R}, \mathbf{B}|\mathbf{x}^b) \mathrm{d}(\mathbf{R}, \mathbf{B})} \tag{2}$$

Here, we assume no prior information on the uncertainty matrices. The distribution $p(\mathbf{R}, \mathbf{B}|\mathbf{x}^b)$ is then uniform. Moreover, the integral in the denominator of the right term of Eq. (2) is computed over all the possible $(\mathbf{R}, \mathbf{B})$. It is then independent of the local $(\mathbf{R}, \mathbf{B})$. Thus, we can deduce from Eq. (2) that:

$$p(\mathbf{R}, \mathbf{B}|\mathbf{y}^0 - \mathbf{H}\mathbf{x}^b, \mathbf{x}^b) \propto p(\mathbf{y}^0 - \mathbf{H}\mathbf{x}^b|\mathbf{R}, \mathbf{B}, \mathbf{x}^b) \tag{3}$$

Then, Eq. (1) becomes:

$$p(\mathbf{x}|\mathbf{y}^0 - \mathbf{H}\mathbf{x}^b, \mathbf{x}^b) \propto \int_{(\mathbf{R},\mathbf{B})} \mathcal{N}(\widetilde{\mathbf{x}^a}, \widetilde{\mathbf{P}^a}) \cdot p(\mathbf{y}^0 - \mathbf{H}\mathbf{x}^b|\mathbf{R}, \mathbf{B}, \mathbf{x}^b) \mathrm{d}(\mathbf{R}, \mathbf{B}) \tag{4}$$

The complete pdf $p(\mathbf{x}|\mathbf{y}^0 - \mathbf{H}\mathbf{x}^b, \mathbf{x}^b)$ finally has the shape of an infinite sum of normal distributions, which are distributed along a Wishart-like distribution (a generalization of χ^2 distributions; Wishart, 1928). There is no reason for the complete pdf to be a Gaussian itself; it cannot be described with only its node and its covariance matrix. In order to properly describe the complete pdf $p(\mathbf{x}|\mathbf{y}^0 - \mathbf{H}\mathbf{x}^b, \mathbf{x}^b)$, we use a Monte-Carlo sampling method following Eq. (4). Sampling a distribution of normal distributions can be burdensome. Indeed, the Monte-Carlo sampling should be, at first sight, an ensemble of Monte-Carlo samplings on all the local normal distributions. Yet, one can note that the normal pdfs within the integral sign in Eq. (4) are symmetric with respect to their node, located to the vector $\widetilde{\mathbf{x}^a}$ associated to the dummy tuple $(\mathbf{R}, \mathbf{B})$. Thus, the complete pdf $p(\mathbf{x}|\mathbf{y}^0 - \mathbf{H}\mathbf{x}^b, \mathbf{x}^b)$ can be sampled with only the local vectors $\widetilde{\mathbf{x}^a}$, thus limiting the total number of needed samples.

Full Screen / Esc

Printer-friendly Version

Interactive Discussion

The last obstacle in the Monte-Carlo sampling is the characterization of the pdf of the uncertainty matrices ($\mathbf{R}, \mathbf{B}$). This distribution of the error statistics is intricate. Nevertheless, its node is located at the Maximum of Likelihood (as developed by Michalak et al., 2005) and it behaves as a χ^2-shaped distribution. This Maximum optimally balances

5 the observation and prior state error variances according to the prior vector $\mathbf{y}^0 - \mathbf{H}\mathbf{x}^b$ (Chapnik et al., 2004). From here, we decide to approximate the complicated distribution of the error statistics by a distribution of diagonal matrices ($\mathbf{R}, \mathbf{B}$). Using a subspace of the possible error statistics can moderate the generality of the method. In particular, no correlation of errors will be included with diagonal uncertainty matrices. Correla-

10 tions can be used in some frameworks to detect the biases in the system (Berchet et al., 2013). Additionnaly, correlations of observation or background errors can indicate redundant pieces of information in the inversion system. An inversion computed with no correlation then tries to use too much information and is expected to give too optimistic a reduction of uncertainties on the fluxes. Nevertheless, in Sect. 3, we reduce

15 the observation and state spaces in order to compute the Monte-Carlo marginalization. Thus, we drastically limit the amount of information used in the system. In this configuration, the correlation issue is then attenuated and the diagonal assumption is valid. For each diagonal term of the ($\mathbf{R}, \mathbf{B}$) tuple, we prescribe a χ^2 distribution, the average of which equals the associated term in the Maximum of Likelihood tuple.

20 A direct algorithm of Maximum of Likelihood (applied to atmospheric inversion in, e.g., Winiarek et al., 2012; Berchet et al., 2013), with no Monte-Carlo sampling, would then provide a good approximation of the node of the posterior pdf we are looking for. But, with such a direct algorithm, the infered pdf would have a wrong shape and erroneously under-estimated uncertainties on the result. At the Maximum of Likelihood, all

25 the pieces of information in the system are considered perfectly usable by the inversion which then gives too optimistic posterior uncertainties in this case. Estimations of the Hessian matrix of the Likelihood at its maximum have been used to deduce better uncertainties on the posterior fluxes (e.g., Michalak et al., 2005; Wu et al., 2013). Hessian matrices are not always sufficient to characterize uncertainties, especially as

the kurtosis of the Monte-Carlo distribution is bigger than the one of a Normal distribution. Following this approach, additional statistical momenta should be used in order to characterize all the posterior uncertainties. The Monte-Carlo approach makes this characterization more straighforward. In Fig. 1, we draw an example of the distribution of the Monte-Carlo posterior vector ensemble along a dimension of the state space. The black curve depicts the posterior distribution inferred with the Maximum of Likelihood, with under-estimated spread compared to the Monte-Carlo distribution. On the opposite, as illustrated by the green curve, a Normal distribution with the same node and the same standard deviation gives a misleading flat shape. As for a Gaussian, we then define the symmetric tolerance interval, so that 68.27% of the samples are in the range (the hatched portion of the histogram in Fig. 1). This interval is equivalent to the gaussian $\pm\sigma$ interval, with σ the standard deviation. One shall remind that the computed tolerance interval does not depict a Normal distribution. A Normal distribution with the same tolerance interval (the red curve in Fig. 1) is still misleadingly flat. In all the following, we will write the tolerance interval TI_{68}, $[x^{low}, x^{high}]$.

To summarize (as represented in the block diagram of Fig. 2), the Maximum of Likelihood is first estimated using a pseudo-Newtonian algorithm, similarly to what has been done in the literature (e.g., Winiarek et al., 2012; Berchet et al., 2013). We deduce from this Maximum of Likelihood the plausible distribution of the uncertainty matrices $(\mathbf{R}, \mathbf{B})$. Through a Monte-Carlo sampling of uncertainty matrices $(\mathbf{R}, \mathbf{B})$ along the deduced distribution, we compute an ensemble of possible posterior vectors $(\widetilde{x^a}_{(\mathbf{R},\mathbf{B})})$. We can then define the tolerance intervals TI_{68} and a posterior covariance matrix filled by the covariances of the ensembles of state components with each others. The explicit definition of this matrix can give valuable information on the ability of the inversion to separate co-located emissions and emissions at different periods and locations. This capacity is used for the evaluation of the OSSEs in Sects. 4.2 and 6.

3 Informed definition of the problem

The general approach defined in Sect. 2 applies a Monte-Carlo method on individual inversions after the completion of a Maximum of Likelihood algorithm. This procedure requires extensive amounts of memory and computation power. For instance, the explicit computation of **H** with a Chemistry-Transport Model (CTM) closely depends on the dimension of the state space: every column of the observation operator needs one model simulation (Bousquet et al., 1999). Additionally, each step of the algorithm relies on matrix products, determinants and inverses. At first sight, all these operations are as many technical issues in high dimension problems. The dimensions of the observation and state spaces should be reduce to damp these issues, but one shall keep resolutions physically relevant for the system we are analyzing. We show in the following that approximations can be reasonably applied to the full-resolution problem while not impacting the quality of the marginalized inversion results. Applying the Monte-Carlo marginalized inversion is then technically feasible in a problem defined with a reduced dimension from the full-dimension physical problem.

3.1 Observation sampling and flux aggregation

In the inversion framework, the straighter way of minimizing the dimension of a problem is to reduce the dimensions of the observation and state space. Aggregating components of the state space and sampling observations are classically used for this purpose. In most studies, the reduction of the problem is carried out arbitrarily. Here, we propose a more objective way to do so.

In the observation space, more and more surface observation sites nowadays provide quasi-continuous measurements (at least a few data points per minute in the data set we use; Sasakawa et al., 2010; Winderlich et al., 2010). For long windows of inversion at the regional scale (of a few weeks or months), such a frequency of acquisition generates a number of pieces of data technically impossible to assimilate all together in our framework. Concerning the fluxes, one shall aim at a characterization

of the fluxes on very fine pixels and at a high temporal resolution. As the window of inversion lengthens and the domain widens, the number of flux unkowns grows expo-nentially. The fluxes are then to be aggregated within regions of aggregation. However, the aggregation can generate large errors (Kaminski et al., 2001; Bocquet et al., 2011),

5 which would mitigate the benefit of the Monte-Carlo marginalized approach compared to more classical ones applied in other atmospheric inversion studies with no aggrega-tion (e.g., variational inversions; Courtier et al., 1994; Bergamaschi et al., 2005; Pison et al., 2009).

Using the formalism from Bocquet et al. (2011), we define a representation ω that

10 encompasses the horizontal and temporal resolution of the fluxes, the choice of the regions of aggregation and the temporal sampling of the observations. The represen-tation ω is defined through two operators $\mathbf{\Pi}_\omega$ and $\mathbf{\Lambda}_\omega$, which projects respectively the full-resolution state and observation space to smaller ones. After the state space pro-jection with $\mathbf{\Pi}_\omega$, the inversion applies corrections on regions of aggregation with fixed

15 emission distributions, instead of on single pixels. The adjoint of this operator, $\mathbf{\Pi}_\omega^T$, then redistributes total emissions on finer scales with the same fixed emission distribution. The choice of $\mathbf{\Pi}_\omega$ impacts both the state vector x and the observation operator $\mathbf{H}$. The observation sampling $\mathbf{\Lambda}_\omega$ can consist in averaging or picking one value per time step (chosen accordingly to the physical resolution inquired into). For instance, one can de-

20 cide to average the observations by day in order to inquire into the synoptic variability of the atmosphere, related to the fluxes at the meso-scale. The observation sampling applies to both the observation vector y^0 and the observation operator $\mathbf{H}$. The observa-tion operator $\mathbf{H}$ computes the contribution from single sources to single observations. The adjoint of the observation sampling, $\mathbf{\Lambda}_\omega^T$, will then redistribute an average or a sam-

25 ple for each chosen time steps along this time step. The redistribution will follow the raw observed temporal profile within the said time step.

At first glance, choosing the aggregation pattern and the sampling protocol can be considered as two independent physical problems. However, as they both influence the dimension of the observation operator $\mathbf{H}$, they cannot be fixed separately. More

explicitely, we can write a formula, which links $\mathbf{\Pi}_\omega$ and $\mathbf{\Lambda}_\omega$. Indeed, our final objective is to compute total posterior fluxes for each aggregated region that are as close as possible to the posterior fluxes from a full-resolution inversion aggregated afterward. That is to say, we want to confine the norm of $x_\omega^a - \mathbf{\Pi}_\omega x_t^a$ with x_ω^a the posterior state vector resolved in the representation ω and x_t^a the posterior state vector computed with a full-resolution representation of the problem. Algebraic manipulations lead to:

$$x_\omega^a - \mathbf{\Pi}_\omega x_t^a = \mathbf{\Pi}_\omega \mathbf{B} \mathcal{E}_\omega (y^0 - \mathbf{H}x^b) \tag{5}$$

where:

$$\mathcal{E}_\omega = \begin{matrix} \mathcal{P}_\omega & \mathbf{H}^T & \mathbf{\Lambda}_\omega^T & \mathcal{S}_\omega^{-1} & \mathbf{\Lambda}_\omega \\ - & \mathbf{H}^T & & \mathcal{S}^{-1} & \end{matrix} \;,$$

$$\mathcal{S} = \mathbf{R} + \mathbf{H}\mathbf{B}\mathbf{H}^T,$$

$$\mathcal{S}_\omega = \mathbf{\Lambda}_\omega \left\{ \mathbf{R} + \mathbf{H}(\mathcal{A}_\omega + \mathcal{P}_\omega \mathbf{B}\mathcal{P}_\omega)\mathbf{H}^T \right\} \mathbf{\Lambda}_\omega^T,$$

$$\mathcal{P}_\omega = (\mathbf{\Pi}_\omega)^T \mathbf{\Pi}_\omega,$$

$$\mathcal{A}_\omega = (\mathbf{I} - \mathcal{P}_\omega)x_t x_t^T (\mathbf{I} - \mathcal{P}_\omega),$$

x_t = the true state of the system,

$\mathbf{I}$ = the identity matrix.

In Eq. (5), $\mathbf{R}$ and $\mathbf{B}$ are the full-resolution matrices of the error statistics. $\mathbf{\Pi}_\omega^T$ extrapolates the fluxes from the aggregated regions to a finer resolution following an a priori repartition. The matrix $\mathcal{P}_\omega$ then redistributes the fluxes over a region with respect to the prior repartition, but keeping the same total emissions on the region.

For the aggregation errors to be limited, $\mathcal{E}_\omega$ must tend towards $\mathbf{0}$. Then, $\mathcal{S}$ and $\mathcal{S}_\omega$ must be as close as possible to each other and the impact of $\mathcal{P}_\omega$ and of the sandwich product with $\mathbf{\Lambda}_\omega$, $\mathbf{\Lambda}_\omega^T(\cdot)\mathbf{\Lambda}_\omega$, must be as small as possible. In Sects. 3.1.1, 3.1.2 and 3.1.3 below, we explain how to reduce these terms. The exact estimation of Eq. (5)

is complicated. In the following, only heuristic aggregation and sampling is chosen. Considering the computer ressources we use, all the principles we define are applied in order to limit the size of the observation space (resp. the state space) to a dimension of roughly 2000 (resp. 1500). The errors intrinsic to the aggregation process and that are unavoidable are controlled so that the benefit from the general marginalization is not wasted. For instance, in the meso-scale Eurasian case study described in Sect. 5, these considerations lead to the aggregation patterns displayed in Figs. 2 and 6.

When the observation and the state space aggregation are chosen, the operator $\mathbf{H}$ can be computed with the so-called "response functions", based on forward simulations of the transport for each state component (Bousquet et al., 1999).

3.1.1 Observation space sampling

The sandwich product with $\mathbf{\Lambda}_{\varpi}$, $\mathbf{\Lambda}_{\varpi}^{T}(\cdot)\mathbf{\Lambda}_{\varpi}$, aggregates the errors in the observation space and diffuses them back within each aggregate along a prescribed temporal profile. For example, it can typically compute the average error per day; then it allocates for each sub-daily dimension an error proportional to the contribution of the related component of $\mathbf{y}^{0}$ to the daily mean. However, a daily averaging would be dominated by the outliers (e.g, singular spikes or night observations when the emissions remain confined close to the surface due to weak vertical mixing) that are generally associated to very high observation errors (due to fine scale mis-representations of the transport and erroneous night vertical mixing). For this reason, we decide to define $\mathbf{\Lambda}_{\varpi}$ as the daily minimum of the observations carried out within a planetary boundary layer higher than 500 m. Below this threshold, the vertical mixing by the model is known to be possibly erroneous (e.g., Berchet et al., 2013). The daily resolution is chosen in order to keep a representation of the transport relevant to the meso-scale expectations on flux characterization. Higher time resolution would not improve the inversion efficiency due to strong within-day temporal correlations of errors (Berchet et al., 2013).

3.1.2 Observational constraints

One can notice that far from the observational constraints, the atmospheric dispersion (depicted by the sandwich product with $\mathbf{H}$, $\mathbf{H}(\cdot)\mathbf{H}^T$) makes the potential errors negligible compared to the errors generated in the areas close to the stations. Indeed, gathering two close hot spots of emissions thousands of km away of the observation sites is not problematic since the air masses coming from the two spots will be well mixed. On the opposite, two hot spots that are as distant from each other as the first two, but close to an observation site, will generate plume-like air masses with a very high sensitivity to the errors of mixing and transport in the model. We use an estimation of the footprints (representing $\mathbf{H}^T$) in order to fix the typical regions constrained by the network and avoid unfortunate grouping. Within these regions, we use a small spatial resolution for the fluxes and the transport and fine aggregation patterns; outside of them, we choose a coarse resolution and large aggregation patterns. An illustration of aggregation patterns in our case study can be looked at in Fig. 6.

3.1.3 Flux aggregation

Some terms in Eq. (5) are directly related to the aggregation of the fluxes. The term $\mathbf{H}\mathcal{A}_\omega\mathbf{H}^T$ depicts the aggregation errors coming from the uncertain distribution and temporal profile of the fluxes within each aggregation region, then transported to the observation sites. It must be close to $\mathbf{0}$. In our application below, this is particularly important for hot spots of emissions the location of which is poorly known. The term $\mathbf{H}\mathcal{P}_\omega\mathbf{B}\mathcal{P}_\omega\mathbf{H}^T$ must be as close as possible to $\mathbf{HBH}^T$. The factors of divergence come from the areas that are not well constrained by the observations. If, within a region of aggregation, a part is upwind the observation sites, while the other is not seen, then the aggregation errors will scatter on the unseen part of the region. The main sources of errors can then be separated into two different types: (1) the resolution/representation type, and (2) the constraint type.

The type-1 errors are mainly related to the resolution of the observation operator. The models consider uniform the fluxes and the simulated atmospheric mixing ratios on a sub-grid basis and neglects sub-grid processus. This discretization contributes to type-1 errors, as "representation" errors (Tolk et al., 2008). Additionnaly, the distribution within each aggregation region is fixed and sub-region re-scaling are forbidden. The fine resolution close to the observation network is bound to confine type-1 errors (e.g., Wu et al., 2011). Additionnally, the representation error is critical for co-located emissions, especially when the typical temporal and spatial scales of these emissions are different. For instance, grouping hot spots from oil extraction emissions with widespread wetland emissions that quickly vary in time is hasardous. We then aggregate the emissions along their typical time and space scale, hence according to the underlying physical process. An in-depth analysis of the footprints and the small patterns of aggregation close to the observation sites should limit the type-2 constraint errors. Area under high observational constraints should not be grouped with under-constrained areas.

The resolution and aggregation choices can be computed objectively, but at a very high cost and only within a framework of prescribed frozen error matrices (Bocquet, 2009; Wu et al., 2011; Koohkan and Bocquet, 2012). For our purpose, we cannot afford such computation costs and rely on heuristic choices: small resolution and aggregation patterns close to the observation sites, aggregation by type of emission, separation of constrained/under-constrained areas by analyzing the footprints. These non-optimal subjective choices may damp the efficiency of our method and must be carried out cautiously.

3.2 Numerical artifacts

In addition to the need of defining a well-sized problem, smart adaptations can be applied to the computation of the method in order to enhance the efficiency of the algorithm. We face several sources of numerical artifacts in the computation of the method. In the pseudo-Newtonian Maximum of Likelihood algorithm, numerical artifacts are

generated by the under-constrained regions. After a few steps, the gradient of the Likelihood is dominated by such regions and the algorithm stays stationary. Such regions can be diagnosed using the diagonal terms of the influence matrix **KH** (following Cardinali et al., 2004). This matrix depicts the sensitivity of the inversion to elementary changes in the observations. Strong observation constraints are related to high sensitivity. After stagnation, the regions with a diagnosed **KH** < 0.5 are then flagged out and the algorithm is carried on. This way, the sufficiently constrained components of the state vector are processed until the algorithm converges. A third to half of the regions are flagged out this way in our case study.

The detection of the mis-representation of hot-spot plumes should also be enhanced. Despite the minimum daily sampling and the fine resolution close to the observation network, the plume issue can still generate temporal and spatial mismatches. For example, a point source can influence a station in the reality, but not in the model because it has been mis-located, and conversely. This creates significant differences between the simulated and the observed concentrations. The Maximum of Likelihood algorithm attributes such mismatches to prior errors and/or observation errors. High diagnosed errors in the Maximum of Likelihood algorithm are then a criterion for plausible mismatches. We know such plumes must be flagged out from the inversion to avoid unrelevantly high influence from very local sources hard to represent. Since we notice that the observation and prior computed errors follow a Fisher-like distribution, we choose to flag out the observations that are within the 95 % tail of the distribution.

4 Validation experiments

In Sect. 2, we describe our modified atmospheric inversion by marginalization. In Sect. 3, we propose some rules to follow in order to properly define the problem. The method has to be validated along objective criteria. In the following, we summarize the general structure of the method (Sect. 4.1) in order to identify the critical points to test in the method. We deduce from these points some Observing System Simulation

Back | Close

Full Screen / Esc

Printer-friendly Version

Interactive Discussion

Experiments to carry out. In Sect. 4.2, we define the scores according to which the method will be evaluated.

4.1 Method summary and test approach

The method described in Sect. 2 and 3 is condensed in the block diagram in Fig. 2. The marginalized inversion takes the same input as any other atmospheric inversion: some atmospheric measurements and prior maps of fluxes with specified resolution and temporal profiles. In Sect. 3, we give recommandations on the processing of the "raw" inputs, so we get an observation vector y^0, a prior state vector x^b and an observation operator $\mathbf{H}$ that are small enough to be computable by the method. These highlights are mainly the sampling of the observations per day (in accordance with our objective of characterizing meso-scale fluxes in our case study) and the aggregation of the fluxes by regions (based on physical consideration and footprint analysis). The Maximum of Likelihood algorithm processes y^0, x^b and $\mathbf{H}$ in order to find a tuple of optimal diagonal error matrices $(\mathbf{R}_{max}, \mathbf{B}_{max})$. This Maximum of Likelihood is found by a Pseudo-Newtonian ascending algorithm. We then infer from $(\mathbf{R}_{max}, \mathbf{B}_{max})$ the approximate shape of the distribution of all the possible error matrices $(\mathbf{R}, \mathbf{B})$. We carry out a Monte-Carlo sampling on these distributions of errors and get an ensemble of posterior state vectors $(\widehat{x^a})$. The processing of this ensemble provides the final output of the method: a tolerance interval TI_{68} of the posterior state and the posterior correlations between the components of the state space. The method also allows the explicit computation of the influence matrix $\mathbf{K}_{max}\mathbf{H}$ in order to analyze the constrained regions of emissions only.

To summarize, the marginalize inversion processes two vectors and one operator: y^0, x^b, and $\mathbf{H}$, as any other atmospheric inversion. The main difference resides into the automatic diagnosis of the error matrices distribution, in contrast with the traditionnal assigning of frozen error matrices based on expert knowledge. Thus, we do not have to inquire into the sensitivity of our method to the prescribed spatial correlations of flux

errors, or to the error variances. Such a sensitivity is transposed to the choice of the aggregation patterns and the sampling protocol, as defined in Sect. 3.1. We show in the following that the chosen configuration of aggregation and the sampling protocole are relevant in our case study. OSSEs are then to be carried out to evaluate the sensitivity of the method to y^0, x^b, $\mathbf{H}$.

We assume that, in our case, the method is not sensitive to errors in y^0. Indeed, in all the following, we consider that the measurement errors are negligible compared to transport errors; this is true for surface sites that fullfill the World Meteorological Organisation strict recommmandations for accuracy and precision (WMO/GAW, 2011). This approximation does not hold for satellite total columns measurements, for which the transport errors are smoothed over the vertical atmospheric column and the instrument errors are higher. Hence, we do not perturb y^0 in order to represent the instrumental uncertainties in the OSSEs.

The OSSEs are then based on perturbations of x^b and $\mathbf{H}$. The discrepancies between the background x^b and the "truth" x^t are of two types: (1) the erroneous distribution of the fluxes within aggregation regions, and (2) incorrect total emissions by region. For example, in Eurasia, the maps of the distribution of the wetlands differ drastically from a database to another (Frey and Smith, 2007). Apart from the distribution, the amount of gas emitted by each process is uncertain, due to mis-parameterizations or, for anthropogenic emissions, mis-specified activity maps (e.g., Rypdal and Winiwarter, 2001). The transport $\mathbf{H}$ differs from the "true" transport mainly because of the resolution of the model, the parameterization of subgrid processes (such as the vertical turbulent mixing in the planetary boundary layer or the deep convection), and the meteorological forcings fields (which are not necessarily optimized for transport applications).

The main sources of errors in the inversion are then: (1) a wrong representation of the transport (highly dependent of the transport model used, its resolution, its parameterization and the exactitude of forcing wind fields), (2) an erroneous distribution of the fluxes within aggregation regions (each inventory and database has different statistical methods and parameters to reproduce surface fluxes), and (3) incorrect total

emissions by regions. In order to evaluate the impact of each point on the inversion result, we carry out OSSEs with perfect synthetic observations from the "true" emissions and "true" transport (defined in the set-up in Sect. 5). We test the ability of the marginalized inversion to reproduce the "true" fluxes or, at least, consistently include the "truth" within the tolerance intervals. There are eight possible combination of correct or perturbed phases of the 3 parameters. The "all true" combinaison is not relevant: then $y^0 - Hx^b = 0$ and the Maximum of Likelihood algorithm is stationary. Seven combinations remain, detailed in Table 1. We run the marginalized inversion for the seven OSSEs and evaluate them along the scores defined in Sect. 4.2.

4.2 Evaluation

We expect an atmospheric inversion to provide reliable ranges of uncertainties for surface fluxes. That is to say, for as many components of the state vector x_i as possible, the "truth" x_i^t should be within the tolerance interval TI_{68}, $[x_i^{low}, x_i^{high}]$ (defined in Sect. 2). In order to evaluate the ability of producing consistent fluxes, we define a relative score z_{rel} for each component of the state vector: $(z_{rel})_i = 2\frac{|x_i^a - x_i^t|}{x_i^{high} - x_i^{low}}$. Hereafter, all the scores will be expressed in % for better readability. Statistically, z_{rel} has no upper bound. Relative scores bigger than 100 % are not statistically inconsistent, but, for the method to be validated, we expect that the proportion of state components with $z_{rel} < 100\%$ is dominant.

Furthermore, the atmospheric inversion is supposed to reveal pieces of information to the understanding of the system. Then, we also expect that a correct relative score below 100 % is not reached by specifying huge tolerance intervals. To evaluate the ability of the marginalization of getting close to the reality, i.e. providing valuable information on the state of the system, we define an absolute score z_{abs}: $(z_{abs})_i = \left|\frac{x_i^a}{x_i^t} - 1\right|$. The smaller the absolute score, the more accurate the marginalized inversion.

An inversion also must be able to evaluate the observation constraints on the regions. An objective estimator of the constraints on the regions is the influence matrix **KH** defined in Sect. 3. The Kalman gain matrix depends on the tuple (**R**, **B**). Amongst all the Monte-Carlo tuples, we compute the influence matrix for the tuple associated to

5 the Maximum of Likelihood. The diagonal terms of this matrix range from 0 to 1. They give for all components of the state space the constraint given by the observations. We then define the influence score: $(z_{\text{infl}})_i = (\mathbf{K}_{\text{max}}\mathbf{H})_i$. The closest to 100 % these terms, the more constraints the inversion provides. We can then deduce the typical range of influence of the observation sites and detect the blind spots of the used network.

10 Another point most inversions do not compute is the typical temporal and spatial scales the inversion can differentiate in the fluxes, considering the atmospheric transport and the density of the observations. Our marginalized inversion gives access to an explicit matrix of correlations as defined in Sect. 3. Strong positive and negative correlations between two components of the state space indicate that the inversion

15 cannot separate the contributions from the two components. For example, air masses observed at a station and coming from two regions upwind the station will have a mixed atmospheric signal difficult to analyse. Co-located emissions are not necessarily differenciated in the atmospheric signal. Moreover, in a regional framework, when a model of limited area is used coupled to lateral boundary conditions (LBC), the inversion must

20 explicitly alert on the regions that cannot be separated from the boundary conditions. In the case of strong correlations in the posterior covariance matrix, it is not relevant to try to infer specific information for the two separate regions. Then, we group the state space components according to their posterior correlations. We define a threshold of correlation r_{max} and associate couple of regions (i, j) such that $|r_{i,j}| > r_{\text{max}}$. If we pre-

25 scribe $r_{\text{max}} = 0$, all the regions will be grouped; on the opposite, if $r_{\text{max}} = 1$, no group will be formed. The optimal correlation threshold is not evident. We test the grouping for all possible r_{max}. We flag out from the processing of the results all the groups, which include some contributions from the LBC. Thus, from this post processing, we only keep the regions that are clearly constrained by the observation sites, with no interference

from the LBC. Moreover, we can infer the spatial and temporal scale that the inversion can resolve from the grouping patterns.

For each possible r_{max} and each component i of the state space, we then have defined 3 indicators:

$$\begin{cases} (z_{\mathrm{rel}})_i = 2\dfrac{|x_i^{\mathrm{a}} - x_i^{\mathrm{t}}|}{x_i^{\mathrm{high}} - x_i^{\mathrm{low}}} \\[2ex] (z_{\mathrm{abs}})_i = \left| \dfrac{x_i^{\mathrm{a}}}{x_i^{\mathrm{t}}} - 1 \right| \\[2ex] (z_{\mathrm{infl}})_i = (\mathbf{K}_{\mathrm{max}}\mathbf{H})_i \end{cases}$$

In Table 1, the three scores are averaged on the whole domain of interest for the optimal correlation threshold r_{max} (as discussed in Sect. 6.1).

5 Set up of the OSSEs

We compute the OSSEs that we described in Sect. 4 in a realistic meso-scale case. We focus on a domain spanning over Eurasia, from Scandinavia to Korea. At this scale, the air masses residence time is typically of ays to a few weeks. This time scale is small compared to the lifetime of methane of 8–10 years in the atmosphere (mainly due to oxydation by OH radicals; Dentener et al., 2003). Hence, the obervation operator can be consider linear. We apply the method on a region characterized by significant fluxes, with colocation of different sources with different emission time-scales: Siberia. We describe the region of interest and the chosen "truth" for the experiments in Sect. 5.1. We use two transport models in order to simulate the atmospheric transport. The technical details on these models are summarized in Sect. 5.2. In Sect. 5.3, we explain how we choose and compute the synthetic observations for our experiments.

Full Screen / Esc

Printer-friendly Version

Interactive Discussion

5.1 Virtual true state x^t

In the region of interest, the emissions of methane are dominated by wetland, anthropogenic (here, mainly related to the oil and gas industry) and wildfire emissions. In Fig. 3, the distributions of the wetlands and of the oil and gas industry in the region are displayed. Anthropogenic emissions of methane in the region are mainly hot spots related to the intense oil and gas industry in the Siberian Lowlands and to the leaks in the distribution system in population centers in the South part of Siberia. Wetland emissions are mainly confined in the lower part of Siberia in the West Siberian plain, half of which is lower than 100 m a.s.l..

The spatial distribution of the associated fluxes is deduced from: (1) EDGAR database v4.2 (http://edgar.jrc.ec.europa.eu) for year 2008 for anthropogenic emissions, (2) LPX-Bern v1.2 process model at a monthly scale for wetland emissions (Spahni et al., 2011), (3) GFED database at daily scale for wildfires (Giglio et al., 2009). The EDGAR inventory uses economic activity maps by sectors and convolves them with emission factors estimated in laboratories or with statistical studies (Olivier et al., 2005). LPX-Bern is an update of process model LPJ-Bern (Spahni et al., 2011). It includes a dynamical simulation of inundated wetland areas, dynamic nitrogen cycle, and dynamic evolution of peatlands (Spahni et al., 2013; Ringeval et al., 2013). The model uses CRU TS 3.21 input data (temperature, precipitation rates, cloud cover, wetdays) and observed atmospheric CO_2 for each year for plant fertilization. GFED v4 is built from burnt area satellite product (MCD64A1). CH_4 emissions at monthly and daily scales are deduced from the burnt areas using the Carnegie-Ames-Stanford-Approach (CASA model; Potter et al., 1993) and emission factors (van der Werf et al., 2010). Wildfire emissions can be very strong and are punctual in time and space; they are then difficult to analyze by the inversion. Wildfires are included as inputs to the marginalized inversion, but are automatically filtered out during the computation. In all the following, we evaluate the OSSEs only in terms of anthropogenic and wetland emissions.

The EDGAR fluxes are given at the yearly scale and the LPX fluxes are calculated at a monthly scale. Additionnally, LPX monthly fluxes exhibit smoothed patterns while wetland emissions can vary drastically from a point to another. We want the virtual "truth" to reproduce the potential spatial and temporal variability of the emissions. To do so, we intensify the spatial and temporal constrasts from the databases to the virtual "truth". We then compute the "true" state vector x^t by perturbing EDGAR emissions on a monthly base and LPX on a weekly base. That is to say: $x^t = \alpha \otimes x^{data}$, with the vector α depicting the scaling factors by state space component, $\otimes$ the convolution operator and x^{data} the emissions from the databases. The perturbations in α from original EDGAR and LPX databases applied to get the "truth" are scaling factors up to 10. These scaling factors could have been chosen randomly. We infer them with a raw inversion using real data. For both anthropogenic and wetland emissions, the scaling factors can significantly differ from a period of inversion to another. We can then evaluate the ability of the marginalized inversion to catch quick variations. The distribution of the scaling factors α is shown in Fig. 4. These factors are plausible, knowing the uncertainties on the wetland emissions and gas leakage (Reshetnikov et al., 2000). Such target scaling factors are at the edge of the validity of the Gaussian assumption and of the positivity of methane fluxes. The ability of the marginalization to recover such correction factors will prove its robustness.

At the meso-scale, we use a CTM (see Sect. 5.2.2) with a limited area domain. Initial and lateral boundary conditions (IC and LBC) are then also to be optimized in the system to correct the atmospheric inflow in the domain. Lateral concentrations are deduced from simulations at the global scale by the general circulation model LMDz with the assimilation of surface observations outside the domain of interest (Bousquet et al., 2006). The LBC are optimized by periods of 10 days. We aggregate the LBC along 4 horizontal components and 2 vertical ones (1013–600 hPa and 600–300 hPa). As for anthropogenic and wetland emissions, we apply the scaling factors α on the components of x^t related to LBC by periods of 10 days.

Full Screen / Esc

Printer-friendly Version

Interactive Discussion

The OSSEs rely on x^b perturbed from x^t, or not. We apply two types of perturbations as summarized in Table 1. In OSSE 1, 4, 5 and 7, we only implement prior fluxes with different total emissions on the regions of aggregation. We take the emissions of the raw inventories as background to test the ability of recovering "true" fluxes from realistic background fluxes without assigning frozen prior errors. In OSSE 2, 4, 6 and 7, the distribution of the prior fluxes is modified from the "truth". We choose all flat flux distributions for each region of aggregation as prior fluxes.

5.2 Simulation of the transport H

We use two different transport models in order to evaluate the impact of the transport on the inversion. We define $\mathbf{H}_{\text{FLEXPART}}$ with the Lagrangian dispersion model FLEXPART and $\mathbf{H}_{\text{CHIMERE}}$ with the Eulerian Chemistry-Transport Model CHIMERE. Any transport model can be considered at some point biased compared with the reality. Confronting the results from FLEXPART to those from CHIMERE will allow us to test the robustness of our method to the biases.

5.2.1 The Lagrangian model: FLEXPART

With the Lagrangian dispersion model FLEXPART (Stohl et al., 2005), we can compute the footprints of the observations, hence $\mathbf{H}^T_{\text{FLEXPART}}$. We use FLEXPART version 8.2.3 to compute numerous back-trajectories of virtual particles from the observation sites. The model is forced by ECMWF ERA-Interim data at an horizontal resolution of $1° \times 1°$, with 60 vertical levels and 3 h temporal resolution. Virtual particles are released in a 3-D box centered around each observation site with a 10 day lifetime backwards in time. The footprints are computed on a $0.5° \times 0.5°$ horizontal grid, following the method of Lin et al. (2003), taking into account the boundary layer height at each particle location. The footprints only have to be convoluted to the emission fields in order to get simulated concentrations at the observation sites. The method for computing the footprints considers that only the particles within the boundary layer are influenced by

surface emissions and that the boundary layer is well-enough mixed to be considered as uniform. The uniform vertical mixing of the mixing layer can generate a bias on the surface simulated concentrations. Such a bias is critical in the classical inversion framework and consequently in the one we describe since all the uncertainties are considered unbiased.

FLEXPART can easily compute an estimation of the adjoint of the full-resolution observation operator before choosing the representation ω. Hence, despite the expectable biases, we use this model to estimate the footprints of the network and deduce the aggregation patterns needed to compute $\mathbf{H}_{CHIMERE}$.

5.2.2 The Eulerian model: CHIMERE

Using the Eulerian mesoscale non-hydrostatic chemistry transport model CHIMERE (Vautard et al., 2001; Menut et al., 2013), we explicitly define the observation operator $\mathbf{H}_{CHIMERE}$ by computing the forward atmospheric transport from the emission aggregated regions (defined according to Sect. 3 criteria) to the observation sites. This model was developed in a framework of air quality simulations (Schmidt et al., 2001; Pison et al., 2007), but is also used for greenhouse gas studies (Broquet et al., 2011; Berchet et al., 2013). We use a quasi-regular horizontal grid zoomed near the observation sites after Sect. 3 considerations. The domain of interest is of limited area and spans over the mainland of the Eurasian continent (see Fig. 3). The average side length of the grid cells near stations is 25 km, while it spans over 150 km away of the observation sites. The 3-D-domain embraces roughly all the troposphere, from the surface to 300 hPa ($\sim$ 9000 m), with 29 layers geometrically spaced. The model time step varies dynamically from 4 to 6 min depending on the maximum wind speed in the domain. The model is an off-line model which needs meteorological fields as forcing. The forcing fields are deduced from interpolated meteorological fields from the European Centre for Medium-range Weather Forecast (ECMWF) with a horizontal resolution of $0.5° \times 0.5°$ every 3 h.

Full Screen / Esc

Printer-friendly Version

Interactive Discussion

5.3 Synthetic observations y^0

We compute synthetic observations from the "true" state vector, with the CTM CHIMERE. That is to say, in all the following, we consider that: $y^0 = H_{CHIMERE} x^t$. The site and date of available observations are chosen according to the operated observation sites in the region. Thirteen Eurasian surface sites have been selected. These sites are maintained by NIES (Tsukuba, Japan; Sasakawa et al., 2010), IAO (Tomsk, Russian Federation), MPI (Iena, Germany; Winderlich et al., 2010), NOAA-ESRL (Boulder, United States of America; Dlugokencky et al., 2009), and KMA (Seoul, Korea). The description of the sites is given in Table 2. The observation sites do not carry out measurements all the year round due to logistical issues and instrument dysfunctions. In order to reproduce this sampling bias, we generate synthetic observations only when real measurements are available from January to December 2010.

6 Results and discussion

After the description of the set-up in Sect. 5, we now have a "true" state x^t and some reference observations y^0. We also have two observation operators $H_{CHIMERE}$ and $H_{FLEXPART}$ and several possible prior fluxes x^b as inputs for the marginalized inversion developed in Sect. 2. In order to evaluate the method, we now carry out the OSSEs described in Table 1 following the complete procedure in Fig. 2. In Sect. 6.1, we examine the average robustness of the method. Then, in Sect. 6.2, we explore the spatial efficiency of the marginalized inversion in our case study. In Sect. 6.3, we discuss the enhancement provided by our method compared to the classical Bayesian framework, despite some limitations.

6.1 Robustness of the method

The marginalization should consistently reproduce the "truth" or, at least, detect its inability in characterizing the fluxes from the given atmospheric contraints. As detailed in Sect. 4.2, the aggregation regions may have strong posterior correlations after the marginalized inversions. This denotes the difficulties that the inversion encounters in separating some emissions. The aggregation regions can be grouped along correlation thresholds r_{max} arbitrarily chosen in order to explicitly take into account the emission dipoles. In Fig. 5, we plot the profiles of the scores defined in Sect. 4.2 along the possible correlation thresholds r_{max} for grouping the regions. Specifying a correlation threshold r_{max} allows identifying the typical temporal and spatial scales that the inversion can separate. In the case of a limited domain CTM, the influence of the LBC and of the inside fluxes can be mis-separated. The correlations take into account this issue and the correlation threshold specifies the tolerance to such mis-separations.

For all OSSEs, the influence score z_{infl} increases with r_{max}. In the correlation processing after the computation of the marginalized inversion, the threshold r_{max} depicts the degree of tolerance to mis-separation between inside fluxes and LBC. The higher the threshold of tolerance r_{max}, the fewer inside fluxes are considered unseparable from the LBC. Hence, fewer aggregation regions are eliminated from the inversion and more fluxes are corrected by the inversion. As the number of constraints increases, we notice that the absolute and relative scores also tend to increase with r_{max}. That is to say, if we only try to get average information on big regions, the posterior fluxes can be expected to be closer to the "truth". On the opposite, if we try to process too much spatial information from the inversion, we must expect more discrepancies with the "truth". In some OSSEs, for wetlands regions, these discrepancies exceed the threshold of consistency of $z_{rel} > 100\%$. One should find a balance between the physical scales one want to separate and the consistency of the results. In Table 1, we summarize the scores of every OSSE for a chosen correlation threshold with respect to result consistency.

Both in Table 1 and Fig. 5, looking at a given correlation threshold r_{max}, one would expect influence, relative and absolute scores that get more wrong when the inversion conditions degrades. The fossil fuel influence score follows this trend: the more perturbed the transport and the prior fluxes, the more state space components are considered un-inversible. The hot-spot regions of emissions are broadly filtered out and the remaining regions can be well characterized by the inversion even with wrong distribution and transport patterns. Some effects in the degrading conditions of the inversion can though compensate each other. For example, the absolute scores of OSSEs 3 and 6 are worse than the scores of OSSEs 5 and 7. The situation for wetland emissions is different. These emissions are smoother than oil and gas emissions and are then not excluded because of wrong transport or distributions. For this reason, the influence score does not exhibit a clear trend with degrading inversion condition.

For wetland regions, transport seems to be the predominant factor of errors. OSSEs 3, 5, 6 and 7 do not consistently reproduce the "truth" with relative scores higher than 100 % when $r_{max} \geq 0.4$. These discrepancies can be attributed to the very high variability prescribed in the "true" wetland emissions. An erroneous transport will fail in detecting brutal changes of emissions at the synoptic scale. The wetland emissions should then be grouped temporally and spatially in order to average the point release of methane. The erroneous tolerance intervals can also be related to the biased transport in FLEXPART compared with CHIMERE. Since we filtered out most of the plumes with spatial and temporal mismatches with the observations, the horizontal biases in the transport are confined. Concerning the vertical bias, a wrong simulated vertical mixing in the planetary boundary will apply on all the fluxes. This bias will then have an impact on the atmospheric concentrations that is relatively smoothed, uniform and constant. Therefore, an accurate detection of such a bias is very difficult. Any inversion relies on the unbiased assumption of the errors. The inversion will attribute the biases to the flux for wetland regions, impacting the result of the inversion. As other inversions, despite the marginalization, it appears that the results on wetland regions may be sensitive to vertical transport biases in the models.

In Fig. 5, one can notice some outlier peaks for low r_{max}. For low r_{max}, very few regions are computed in the inversion. The peaks are created by the regions that are not anymore considered as mis-separated with the LBC when r_{max} increases. For some OSSEs, these newly computed regions have very wrong scores and dominates upon the other few computed regions. For this reason, one should be very careful in the chosen correlation threshold. In order to avoid the score unstability, the optimum threshold should be chosen higher than 0.4. Above 0.5, as described above, the inversion is limited by the temporal and spacial variability of the fluxes to optimize and by the transport biases. Then, it can not reach the requirement of consistent reproduced fluxes.

Thus, the marginalized inversion seems sensitive to transport biases and to fluxes varying too quickly, as any other inversions. Nevertheless, a post-processing is made possible by the explicit computation of the posterior covariances and of the influence matrix. This post-processing proves that the atmospheric inversion is not able to inquire into very fine scales in our case study. The correlation grouping of un-differenciable regions allows an accurate analysis of the best possible signal detectable by the inversion. In the following, we take a correlation threshold of 0.5 as a good balance between sufficient constraints on the system and consistent posterior fluxes.

6.2 Spatial evaluation

We have chosen a threshold of correlation grouping the regions so that the averaged scores on the whole domain of interest are optimal. The scores are not uniformly distributed. In Fig. 6, the distributions of the three scores are displayed for fossil fuel regions and wetlands for OSSE 1 (transport and distribution of the fluxes same as the "truth", perturbed masses by regions; see Table 1). We choose the "easiest" OSSE configuration in order to evaluate the behaviour of the marginalized inversion in the best configuration possible, thus getting the upper bound for the expectable quality of the results. Any realistic set-up is likely to give worse results. In the figure, the scores are projected on the aggregation grid built on the considerations in Sect. 3. Most of the observation sites are located in the center of the domain (see Fig. 3). Then, the influence

Printer-friendly Version

Interactive Discussion

score is on average better close to the core of the network for the wetlands. For the fossil fuel regions, the influence score is relatively high also upwind the monitoring network (dominant winds blow west to east in the region). Additionnally to the network density, the inversion suffers from mis-separation of side regions and LBC. For this reason, side regions tend to be less constrained than center ones. However, one can notice in both wetland and fossil fuel maps that some center regions are significantly less constrained than the core of the domain on average. These are regions of very high and dense emissions close to the observation sites (< 500 km). The air masses coming from these regions to the observation sites are plume shaped air masses. The inversion has troubles in assimilating single plumes. In Sect. 3, filters have been implemented in order to detect these problematic regions. The marginalized inversion effectively filtered out these regions.

The absolute and relative scores show unexpected patterns. Scandinavia and China regions own some of the lowest absolute and relative scores. These two side regions are filtered out most of the time because of strong correlations with the LBC components of the state space (confirmed by their low influence score). Consequently, when not filtered out, these regions are very well and unambiguously constrained, so the good relative and absolute scores. For the rest of the domain, the scores are mostly the best, the closest to the observation network.

6.3 Limitations and benefits

The marginalized inversion provides an objectified quantification of the errors in the inversion system. With the Monte-Carlo approach we implemented, we are able to consistently take into account the sources of uncertainties in the inversion process, especially those from the prescribed error covariance matrices. As evaluated through OSSEs, the method proved to consistently catch "true" fluxes on average in the particular Siberian set-up. Moreover, the Siberian set-up is a difficult case study for the atmospheric inversion, with co-located intense fluxes that vary at temporal and spatial scales smaller than the meso-scale. The processing of hot-spots, critical in most

inversion configurations, is consistently managed, through filters on the plume-shaped air masses. An in-depth analysis of the temporal variability of the fluxes will be carried out in a future work with the Siberian set-up and real observations. Additionnaly, as a comparison, we carried out the same OSSEs on the same particular Siberian set-up, but with expert-knowledge frozen error matrices. The correlation profiles and the spatial structures of the scores with the expert-knowledge matrices are not shown because the general patterns are very similar to what is described for the marginalized inversion. The patterns are similar, but the values of the scores are significantly depreciated from the marginalized inversion to the expert-knowledge one. The expert-knowledge relative and absolute scores are several times bigger than the ones from the marginalized inversion, thus statistically incompatible with the "truth".

The marginalized inversion explicitly computes the posterior covariance matrix and the influence matrix. The physical interpretation of the inversion results are then enhanced by a clear analysis of the observation constraints to the fluxes. The processing of the posterior correlations makes the detection of the dipoles and un-distinguishable regions possible. The influence of the lateral boundary conditions, specific to the mesoscale and the use of limited area CTMs, is estimated. Thus, the regions upwind the observation sites and mixed with lateral air masses can be excluded from the inversion. From the correlations, the grouping of regions gives an estimate of the typical spatial and temporal scale the method can compute. In our case, with few and distant observation sites, the groups of regions cover very large areas. Thus, a grid-point high resolution inversion would not have given deep insights into the fluxes we are looking at.

Despite all these benefits compared with the classical Bayesian framework, our method still has limitations. The technical implementation of the method needs extensive computation power and memory requirements. For this reason, we have to drastically reduce the size of the problem to solve. The size reduction relies on rigourous considerations difficult to compute. We then applied heuristic principles in order to choose the aggregation patterns of the observations and the fluxes. This subjective procedure

can modify the results of the inversion and must be carried out very cautiously. The way we group the regions after the marginalized inversion in order to physically interpret the results is also subjective. We choose a correlation threshold of 0.5 in order to counter-balance the need of useful constraints from the inversion and the requirements of consistently reproducing the "true" fluxes. Other thresholds could have been chosen and the typical distinguishable temporal and spatial scales would slightly differ from one threshold to another. But, in any chosen correlation threshold, we notice that most aggregation regions are grouped within bigger ensembles, suggesting that the chosen aggregation patterns are small enough to have reduced impact on the inversion post-processed results.

The marginalized inversion suffers from transport biases as any other inversion. However, the Maximum of Likelihood algorithm considers the biases as random errors and includes them into the error matrix $\mathbf{R}_{max}$. The biases are then taken into account in the marginalized inversion, though as random errors. Biases can be represented, or at least detected, with non-diagonal matrices as suggested by Berchet et al. (2013), but a non-diagonal framework would make the computation of the marginalized inversion critically complicated. In addition to the implicit inclusion of the biases as random error in $\mathbf{R}_{max}$, we reduced the impact of the horizontal transport biases through filters on the plume-shaped air masses. The vertical biases are smoother and more difficult to detect. This issue must be inquired into in further works.

7 Conclusions

At the meso-scale, inconsistencies between inversion configurations appear in the classical Bayesian framework. One of the main sources of inconsistencies is the specification of the error matrices and the non inclusion of the remanent uncertainties on these matrices. We developed a new Bayesian method of inversion from the classical Bayesian framework based on a marginalization on the error matrices and an objectified specification of the probability density function of the error matrices. This method

needs very high computation power and memory ressources. To avoid technical limitations, we reduced the size of the problem by agglomerating the fluxes by region, following objective principles for reducing aggregation errors. We test this method through OSSEs on methane in a domain of interest spanning over Eurasia with significant emissions of different types and different time and space scales. The OSSEs are based on synthetic observations generated from a virtual truth. We evaluate the consistency and robustness of the method on OSSEs with inversion configurations from the more favorable to the most disadvantageous one (perturbed atmospheric transport, flat flux distribution and wrong total masses). The method produces very consistent and satisfactory results. In most cases, the tolerance intervals given by the inversion include the "true" fluxes and the results remain close to the "truth". The method also provides an explicit computation of the constraints on the regions and allows flagging out regions critically mis-separated from the lateral boundary condition. We hence have developed a robust and objectified method able to consistently catch "true" greenhouse gas emissions at the meso-scale and to explicitly group the regions that are physically un-distinguishale with the atmospheric signal only. In addition, we have a method that explicitly produces posterior tolerance intervals on the optimal distinguishable time and space flux scales and that computes the observation network influence on the fluxes.

The robustness of our method on the Siberian case with a biased transport prove it can be generically applied to other meso-scale frameworks. The high spatial and temporal variability of the fluxes in Siberia ensures the possibility of using the system in "easier" inversion set-up. Actual observation from the sites we used for the validation of the method will be exploited in further steps of our work in order to quantify the "real" methane fluxes in the Siberian Lowlands.

References

Ahmadov, R., Gerbig, C., Kretschmer, R., Koerner, S., Neininger, B., Dolman, A. J., and Sarrat, C.: Mesoscale covariance of transport and CO_2 fluxes: evidence from observations and simulations using the WRF-VPRM coupled atmosphere-biosphere model, J. Geophys. Res.-Atmos., 112, D22107, doi:10.1029/2007JD008552, 2007. 4783

Amante, C. and Eakins, B. W.: ETOPO1 1 Arc-minute Global Relief Model: Procedures, Data Sources and Analysis, US Department of Commerce, National Oceanic and Atmospheric Administration, National Environmental Satellite, Data, and Information Service, National Geophysical Data Center, Marine Geology and Geophysics Division, 2009. 4824

Berchet, A., Pison, I., Chevallier, F., Bousquet, P., Conil, S., Geever, M., Laurila, T., Lavrič, J., Lopez, M., Moncrieff, J., Necki, J., Ramonet, M., Schmidt, M., Steinbacher, M., and Tarniewicz, J.: Towards better error statistics for atmospheric inversions of methane surface fluxes, Atmos. Chem. Phys., 13, 7115–7132, doi:10.5194/acp-13-7115-2013, 2013. 4784, 4786, 4787, 4791, 4803, 4810

Bergamaschi, P., Krol, M., Dentener, F., Vermeulen, A., Meinhardt, F., Graul, R., Ramonet, M., Peters, W., and Dlugokencky, E. J.: Inverse modelling of national and European CH_4 emissions using the atmospheric zoom model TM5, Atmos. Chem. Phys., 5, 2431–2460, doi:10.5194/acp-5-2431-2005, 2005. 4784, 4789

Bergamaschi, P., Krol, M., Meirink, J. F., Dentener, F., Segers, A., van Aardenne, J., Monni, S., Vermeulen, A. T., Schmidt, M., Ramonet, M., Yver, C., Meinhardt, F., Nisbet, E. G., Fisher, R. E., O'Doherty, S., and Dlugokencky, E. J.: Inverse modeling of European CH_4 emissions 2001–2006, J. Geophys. Res., 115, D22309, doi:10.1029/2010JD014180, 2010. 4779, 4784

Bergamaschi, P., Houweling, S., Segers, A., Krol, M., Frankenberg, C., Scheepmaker, R. A., Dlugokencky, E., Wofsy, S. C., Kort, E. A., Sweeney, C., Schuck, T., Brenninkmeijer, C., Chen, H., Beck, V., and Gerbig, C.: Atmospheric CH_4 in the first decade of the 21st century:

inverse modeling analysis using SCIAMACHY satellite retrievals and NOAA surface measurements, J. Geophys. Res.-Atmos., 118, 7350–7369, doi:10.1002/jgrd.50480, 2013. 4780

Bocquet, M.: Toward optimal choices of control space representation for geophysical data assimilation, Mon. Weather Rev., 137, 2331–2348, 2009. 4793

5 Bocquet, M., Wu, L., and Chevallier, F.: Bayesian design of control space for optimal assimilation of observations. Part I: Consistent multiscale formalism, Q. J. Roy. Meteor. Soc., 137, 1340–1356, 2011. 4789

Bousquet, P., Ciais, P., Peylin, P., Ramonet, M., and Monfray, P.: Inverse modeling of annual atmospheric CO_2 sources and sinks: 1. Method and control inversion, J. Geophys. Res.-
10 Atmos., 104, 26161–26178, 1999. 4788, 4791

Bousquet, P., Ciais, P., Miller, J. B., Dlugokencky, E. J., Hauglustaine, D. A., Prigent, C., van der Werf, G. R., Peylin, P., Brunke, E.-G., Carouge, C., Langenfelds, R. L., Lathière, J., Papa, F., Ramonet, M., Schmidt, M., Steele, L. P., Tyler, S. C., and White, J.: Contribution of anthropogenic and natural sources to atmospheric methane variability, Nature, 443, 439–443, 2006.
15 4779, 4801

Broquet, G., Chevallier, F., Rayner, P., Aulagnier, C., Pison, I., Ramonet, M., Schmidt, M., Vermeulen, A. T., and Ciais, P.: A European summertime CO_2 biogenic flux inversion at mesoscale from continuous in situ mixing ratio measurements, J. Geophys. Res.-Atmos., 116, D23303, doi:10.1029/2011JD016202, 2011. 4803

20 Cardinali, C., Pezzulli, S., and Andersson, E.: Influence-matrix diagnostic of a data assimilation system, Q. J. Roy. Meteor. Soc., 130, 2767–2786, 2004. 4794

Chapnik, B., Desroziers, G., Rabier, F., and Talagrand, O.: Properties and first application of an error-statistics tuning method in variational assimilation, Q. J. Roy. Meteor. Soc., 130, 2253–2275, 2004. 4786

25 Chevallier, F., Viovy, N., Reichstein, M., and Ciais, P.: On the assignment of prior errors in Bayesian inversions of CO_2 surface fluxes, Geophys. Res. Lett., 33, L13802, doi:10.1029/2006GL026496, 2006. 4784

Ciais, P., Sabine, C., Govindasamy, B., Bopp, L., Brovkin, V., Canadell, J., Chhabra, A., DeFries, R., Galloway, J., and Heimann, M.: Chapter 6: carbon and other biogeochemical cy-
30 cles, in: Climate Change, IPCC, 2–3, 486–514, 2013. 4779

Courtier, P., Thépaut, J.-N., and Hollingsworth, A.: A strategy for operational implementation of 4D-Var, using an incremental approach, Q. J. Roy. Meteor. Soc., 120, 1367–1387, 1994. 4789

Title Page

Abstract | Introduction

Conclusions | References

Tables | Figures

◄ | ►

◄ | ►

Back | Close

Full Screen / Esc

Printer-friendly Version

Interactive Discussion

Cressot, C., Chevallier, F., Bousquet, P., Crevoisier, C., Dlugokencky, E. J., Fortems-Cheiney, A., Frankenberg, C., Parker, R., Pison, I., Scheepmaker, R. A., Montzka, S. A., Krummel, P. B., Steele, L. P., and Langenfelds, R. L.: On the consistency between global and regional methane emissions inferred from SCIAMACHY, TANSO-FTS, IASI and surface measurements, Atmos. Chem. Phys., 14, 577–592, 2014, http://www.atmos-chem-phys.net/14/577/2014/. 4784

Dee, D. P.: Bias and data assimilation, Q. J. Roy. Meteor. Soc., 131, 3323–3343, 2005. 4784

Denning, A. S., Holzer, M., Gurney, K. R., Heimann, M., Law, R. M., Rayner, P. J., Fung, I. Y., Fan, S.-M., Taguchi, S., Friedlingstein, P., Balkanski, Y., Taylor, J., Maiss, M., and Levin, I.: Three-dimensional transport and concentration of SF6, Tellus B, 51, 266–297, 1999. 4783

Dentener, F., Peters, W., Krol, M., Van Weele, M., Bergamaschi, P., and Lelieveld, J.: Interannual variability and trend of CH_4 lifetime as a measure for OH changes in the 1979–1993 time period, J. Geophys. Res., 108, 4442, doi:10.1029/2002JD002916, 2003. 4799

Dlugokencky, E. J., Steele, L. P., Lang, P. M., and Masarie, K. A.: The growth rate and distribution of atmospheric methane, J. Geophys. Res.-Atmos., 99, 17021–17043, 1994. 4779

Dlugokencky, E. J., Bruhwiler, L., White, J. W. C., Emmons, L. K., Novelli, P. C., Montzka, S. A., Masarie, K. A., Lang, P. M., Crotwell, A. M., Miller, J. B., and Gatti, L. V.: Observational constraints on recent increases in the atmospheric CH_4 burden, Geophys. Res. Lett., 36, L18803, doi:10.1029/2009GL039780, 2009. 4779, 4804

Enting, I. G.: Inverse Problems in Atmospheric Constituent Transport, Cambridge University Press, 2002. 4780, 4782

Enting, I. G., Trudinger, C. M., Francey, R. J., and Granek, H.: Synthesis Inversion of Atmospheric CO_2 using the GISS Tracer Transport Model, Tech. Rep. 29, Division of Atmospheric Research Technical Paper, CSIRO, Australia, 1993. 4780, 4783

Frey, K. E. and Smith, L. C.: How well do we know northern land cover? Comparison of four global vegetation and wetland products with a new ground-truth database for West Siberia, Global Biogeochem. Cy., 21, GB1016, doi:10.1029/2006GB002706, 2007. 4796

Geels, C., Gloor, M., Ciais, P., Bousquet, P., Peylin, P., Vermeulen, A. T., Dargaville, R., Aalto, T., Brandt, J., Christensen, J. H., Frohn, L. M., Haszpra, L., Karstens, U., Rundefined"odenbeck, C., Ramonet, M., Carboni, G., and Santaguida, R.: Comparing atmospheric transport models for future regional inversions over Europe - Part 1: mapping the atmospheric CO_2 signals, Atmos. Chem. Phys., 7, 3461–3479, 2007, http://www.atmos-chem-phys.net/7/3461/2007/. 4780, 4784

Title Page

Abstract | Introduction

Conclusions | References

Tables | Figures

|◄ | ►|

◄ | ►

Back | Close

Full Screen / Esc

Printer-friendly Version

Interactive Discussion

Giglio, L., Loboda, T., Roy, D. P., Quayle, B., and Justice, C. O.: An active-fire based burned area mapping algorithm for the MODIS sensor, Remote Sens. Environ., 113, 408–420, 2009. 4800

Gurney, K. R., Law, R. M., Denning, A. S., Rayner, P. J., Baker, D., Bousquet, P., Bruhwiler, L., Chen, Y.-H., Ciais, P., Fan, S., Fung, I. Y., Gloor, M., Heimann, M., Higuchi, K., John, J., Maki, T., Maksyutov, S., Masarie, K., Peylin, P., Prather, M., Pak, B. C., Randerson, J., Sarmiento, J., Taguchi, S., Takahashi, T., and Yuen, C.-W.: Towards robust regional estimates of CO_2 sources and sinks using atmospheric transport models, Nature, 415, 626–630, 2002. 4780

Hargreaves, K. J. and Fowler, D.: Quantifying the effects of water table and soil temperature on the emission of methane from peat wetland at the field scale, Atmos. Environ., 32, 3275–3282, 1998. 4781

Kaminski, T., Rayner, P. J., Heimann, M., and Enting, I. G.: On aggregation errors in atmospheric transport inversions, J. Geophys. Res., 105, 4703–4715, 2001. 4789

Kirschke, S., Bousquet, P., Ciais, P., Saunois, M., Canadell, J. G., Dlugokencky, E. J., Bergamaschi, P., Bergmann, D., Blake, D. R., Bruhwiler, L., Cameron-Smith, P., Castaldi, S., Chevallier, F., Feng, L., Fraser, A., Heimann, M., Hodson, E. L., Houweling, S., Josse, B., Fraser, P. J., Krummel, P. B., Lamarque, J.-F., Langenfelds, R. L., Le Quéré, C., Naik, V., O'Doherty, S., Palmer, P. I., Pison, I., Plummer, D., Poulter, B., Prinn, R. G., Rigby, M., Ringeval, B., Santini, M., Schmidt, M., Shindell, D. T., Simpson, I. J., Spahni, R., Steele, L. P., Strode, S. A., Sudo, K., Szopa, S., van der Werf, G. R., Voulgarakis, A., van Weele, M., Weiss, R. F., Williams, J. E., and Zeng, G.: Three decades of global methane sources and sinks, Nat. Geosci., 6, 813–823, 2013. 4780

Koohkan, M. R. and Bocquet, M.: Accounting for representativeness errors in the inversion of atmospheric constituent emissions: application to the retrieval of regional carbon monoxide fluxes, Tellus B, 64, 19047, doi:10.3402/tellusb.v64i0.19047, 2012. 4793

Lauvaux, T. and Davis, K. J.: Planetary boundary layer errors in mesoscale inversions of column-integrated CO_2 measurements, J. Geophys. Res.-Atmos., 119, 490–508, 2014. 4784

Lauvaux, T., Pannekoucke, O., Sarrat, C., Chevallier, F., Ciais, P., Noilhan, J., and Rayner, P. J.: Structure of the transport uncertainty in mesoscale inversions of CO_2 sources and sinks using ensemble model simulations, Biogeosciences, 6, 1089–1102, doi:10.5194/bg-6-1089-2009, 2009. 4783

Lehner, B. and Döll, P.: Development and validation of a global database of lakes, reservoirs and wetlands, J. Hydrol., 296, 1–22, 2004. 4824

Title Page

Abstract | Introduction

Conclusions | References

Tables | Figures

|◄ | ►|

◄ | ►

Back | Close

Full Screen / Esc

Printer-friendly Version

Interactive Discussion

Lin, J. C., Gerbig, C., Wofsy, S. C., Andrews, A. E., Daube, B. C., Davis, K. J., and Grainger, C. A.: A near-field tool for simulating the upstream influence of atmospheric observations: the Stochastic Time-Inverted Lagrangian Transport (STILT) model, J. Geophys. Res.-Atmos., 108, 4493, doi:10.1029/2002JD003161, 2003. 4802

5 Locatelli, R., Bousquet, P., Chevallier, F., Fortems-Cheney, A., Szopa, S., Saunois, M., Agusti-Panareda, A., Bergmann, D., Bian, H., Cameron-Smith, P., Chipperfield, M. P., Gloor, E., Houweling, S., Kawa, S. R., Krol, M., Patra, P. K., Prinn, R. G., Rigby, M., Saito, R., and Wilson, C.: Impact of transport model errors on the global and regional methane emissions estimated by inverse modelling, Atmos. Chem. Phys., 13, 9917–9937, doi:10.5194/acp-13-
10 9917-2013, 2013. 4783

Macdonald, J. A., Fowler, D., Hargreaves, K. J., Skiba, U., Leith, I. D., and Murray, M. B.: Methane emission rates from a northern wetland; response to temperature, water table and transport, Atmos. Environ., 32, 3219–3227, 1998. 4781

Menut, L., Bessagnet, B., Khvorostyanov, D., Beekmann, M., Blond, N., Colette, A., Coll, I.,
15 Curci, G., Foret, G., Hodzic, A., Mailler, S., Meleux, F., Monge, J.-L., Pison, I., Siour, G., Turquety, S., Valari, M., Vautard, R., and Vivanco, M. G.: CHIMERE 2013: a model for regional atmospheric composition modelling, Geosci. Model Dev., 6, 981–1028, doi:10.5194/gmd-6-981-2013, 2013. 4803

Michalak, A. M., Hirsch, A., Bruhwiler, L., Gurney, K. R., Peters, W., and Tans, P. P.: Maximum
20 likelihood estimation of covariance parameters for Bayesian atmospheric trace gas surface flux inversions, J. Geophys. Res.-Atmos., 110, D24107, doi:10.1029/2005JD005970, 2005. 4780, 4786

Olivier, J. G. J., Van Aardenne, J. A., Dentener, F. J., Pagliari, V., Ganzeveld, L. N., and Peters, J. A. H. W.: Recent trends in global greenhouse gas emissions:regional trends 1970–
25 2000 and spatial distributionof key sources in 2000, Environm. Sci., 2, 81–99, 2005. 4800

Peylin, P., Baker, D., Sarmiento, J., Ciais, P., and Bousquet, P.: Influence of transport uncertainty on annual mean and seasonal inversions of atmospheric CO_2 data, J. Geophys. Res., 107, 4385, doi:10.1029/2001JD000857, 2002. 4784

Peylin, P., Law, R. M., Gurney, K. R., Chevallier, F., Jacobson, A. R., Maki, T., Niwa, Y., Pa-
30 tra, P. K., Peters, W., Rayner, P. J., Rödenbeck, C., van der Laan-Luijkx, I. T., and Zhang, X.: Global atmospheric carbon budget: results from an ensemble of atmospheric CO_2 inversions, Biogeosciences, 10, 6699–6720, doi:10.5194/bg-10-6699-2013, 2013. 4780

Pison, I., Menut, L., and Bergametti, G.: Inverse modeling of surface NO$_x$ anthropogenic emission fluxes in the Paris area during the Air Pollution Over Paris Region (ESQUIF) campaign, J. Geophys. Res., 112, D24302, doi:10.1029/2007JD008871, 2007. 4803

Pison, I., Bousquet, P., Chevallier, F., Szopa, S., and Hauglustaine, D.: Multi-species inversion of CH$_4$, CO and H$_2$ emissions from surface measurements, Atmos. Chem. Phys., 9, 5281–5297, doi:10.5194/acp-9-5281-2009, 2009. 4789

Potter, C. S., Randerson, J. T., Field, C. B., Matson, P. A., Vitousek, P. M., Mooney, H. A., and Klooster, S. A.: Terrestrial ecosystem production: a process model based on global satellite and surface data, Global Biogeochem. Cy., 7, 811–841, 1993. 4800

Reshetnikov, A. I., Paramonova, N. N., and Shashkov, A. A.: An evaluation of historical methane emissions from the Soviet gas industry, J. Geophys. Res.-Atmos., 105, 3517–3529, 2000. 4801

Ringeval, B., Houweling, S., van Bodegom, P. M., Spahni, R., van Beek, R., Joos, F., and Röckmann, T.: Methane emissions from floodplains in the Amazon Basin: challenges in developing a process-based model for global applications, Biogeosciences, 11, 1519–1558, doi:10.5194/bg-11-1519-2014, 2014. 4800

Rypdal, K. and Winiwarter, W.: Uncertainties in greenhouse gas emission inventories – evaluation, comparability and implications, Environ. Sci. Policy, 4, 107–116, 2001. 4796

Sasakawa, M., Shimoyama, K., Machida, T., Tsuda, N., Suto, H., Arshinov, M., Davydov, D., Fofonov, A., Krasnov, O., Saeki, T., Koyama, Y., and Maksyutov, S.: Continuous measurements of methane from a tower network over Siberia, Tellus B, 62, 403–416, 2010. 4781, 4788, 4804

Schmidt, H., Derognat, C., Vautard, R., and Beekmann, M.: A comparison of simulated and observed ozone mixing ratios for the summer of 1998 in Western Europe, Atmos. Environ., 35, 6277–6297, 2001. 4803

Seinfeld, J. H. and Pandis, S. N.: Atmospheric Chemistry and Physics: from Air Pollution to Climate Change, 2nd edn., John Wiley & Sons, Inc., 2006. 4779

Spahni, R., Wania, R., Neef, L., van Weele, M., Pison, I., Bousquet, P., Frankenberg, C., Foster, P. N., Joos, F., Prentice, I. C., and van Velthoven, P.: Constraining global methane emissions and uptake by ecosystems, Biogeosciences, 8, 1643–1665, doi:10.5194/bg-8-1643-2011, 2011. 4800

Title Page

Abstract | Introduction

Conclusions | References

Tables | Figures

|◄ | ►|

◄ | ►
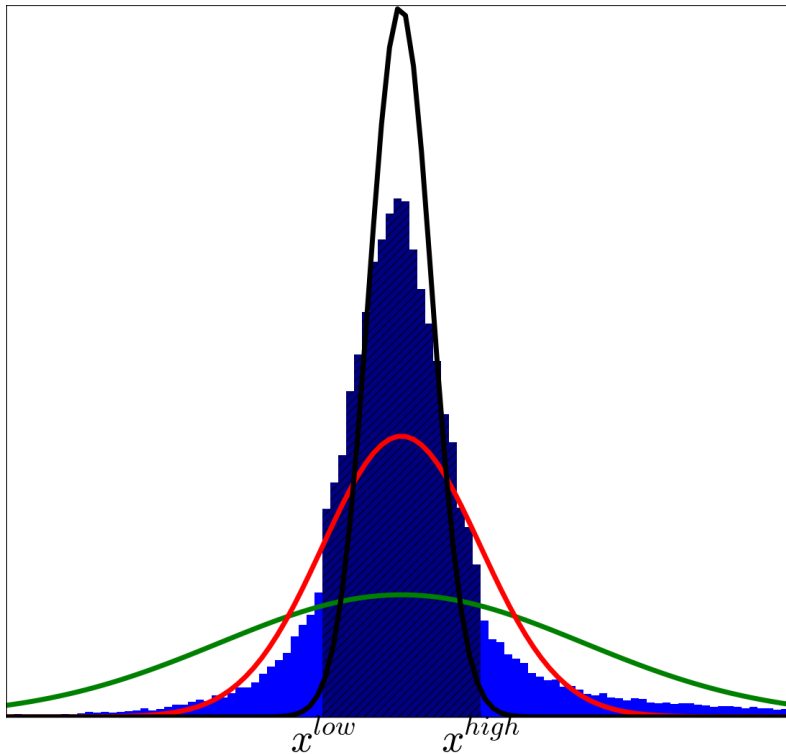
Back | Close

Full Screen / Esc

Printer-friendly Version

Interactive Discussion

Spahni, R., Joos, F., Stocker, B. D., Steinacher, M., and Yu, Z. C.: Transient simulations of the carbon and nitrogen dynamics in northern peatlands: from the Last Glacial Maximum to the 21st century, Clim. Past, 9, 1287–1308, doi:10.5194/cp-9-1287-2013, 2013. 4800

Stohl, A., Forster, C., Frank, A., Seibert, P., and Wotawa, G.: Technical note: The Lagrangian particle dispersion model FLEXPART version 6.2, Atmos. Chem. Phys., 5, 2461–2474, doi:10.5194/acp-5-2461-2005, 2005. 4802

Tarantola, A.: Inverse Problem Theory, Elsevier, New York, 1987. 4780, 4782

Tolk, L. F., Meesters, A. G. C. A., Dolman, A. J., and Peters, W.: Modelling representation errors of atmospheric CO_2 mixing ratios at a regional scale, Atmos. Chem. Phys., 8, 6587–6596, doi:10.5194/acp-8-6587-2008, 2008. 4793

van der Werf, G. R., Randerson, J. T., Giglio, L., Collatz, G. J., Mu, M., Kasibhatla, P. S., Morton, D. C., DeFries, R. S., Jin, Y., and van Leeuwen, T. T.: Global fire emissions and the contribution of deforestation, savanna, forest, agricultural, and peat fires (1997–2009), Atmos. Chem. Phys., 10, 11707–11735, doi:10.5194/acp-10-11707-2010, 2010. 4800

Vautard, R., Beekmann, M., Roux, J., and Gombert, D.: Validation of a hybrid forecasting system for the ozone concentrations over the Paris area, Atmos. Environ., 35, 2449–2461, 2001. 4803

Williams, I. N., Riley, W. J., Torn, M. S., Biraud, S. C., and Fischer, M. L.: Biases in regional carbon budgets from covariation of surface fluxes and weather in transport model inversions, Atmos. Chem. Phys. Discuss., 13, 19051–19083, doi:10.5194/acpd-13-19051-2013, 2013. 4784

Winderlich, J., Chen, H., Gerbig, C., Seifert, T., Kolle, O., Lavrič, J. V., Kaiser, C., Höfer, A., and Heimann, M.: Continuous low-maintenance CO_2/CH_4/H_2O measurements at the Zotino Tall Tower Observatory (ZOTTO) in Central Siberia, Atmos. Meas. Tech., 3, 1113–1128, doi:10.5194/amt-3-1113-2010, 2010. 4781, 4788, 4804

Winiarek, V., Bocquet, M., Saunier, O., and Mathieu, A.: Estimation of errors in the inverse modeling of accidental release of atmospheric pollutant: application to the reconstruction of the cesium-137 and iodine-131 source terms from the Fukushima Daiichi power plant, J. Geophys. Res.-Atmos., 117, D05122, doi:10.1029/2011JD016932, 2012. 4786, 4787

Wishart, J.: The generalised product moment distribution in samples from a normal multivariate population, Biometrika, 20A, 32–52, doi:10.2307/2331939, 1928. 4785

WMO/GAW: 16th WMO/IAEA Meeting on Carbon Dioxide, Other Greenhouse Gases, and Related Measurement Techniques (GGMT-2011), Tech. Rep. 206, World Meteorological Organization Global Atmospheric Watch, Wellington, New Zealand, 2011. 4796

Wu, L., Bocquet, M., Lauvaux, T., Chevallier, F., Rayner, P., and Davis, K.: Optimal representation of source-sink fluxes for mesoscale carbon dioxide inversion with synthetic data, J. Geophys. Res., 116, D21304, doi:10.1029/2011JD016198, 2011. 4793

Wu, L., Bocquet, M., Chevallier, F., Lauvaux, T., and Davis, K.: Hyperparameter estimation for uncertainty quantification in mesoscale carbon dioxide inversions, Tellus B, 65, 20894, doi:10.3402/tellusb.v65i0.20894, 2013. 4786
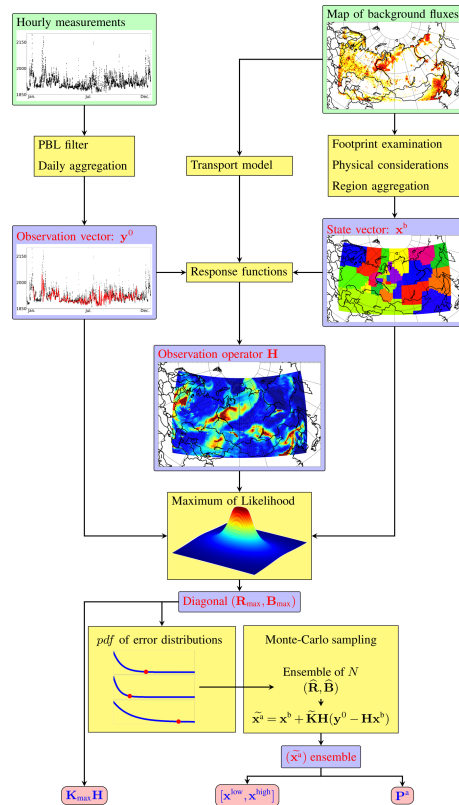
Title Page

Abstract | Introduction

Conclusions | References

Tables | Figures

Back | Close

Full Screen / Esc

Printer-friendly Version

Interactive Discussion

Table 1. OSSEs summary. Three parameters of the inversion (sub-total masses emitted per regions, emission distribution and transport) can be perturbed compared with the "truth". The seven possible combinations are depicted by = and ≠ signs for each parameter and each OSSE. Every OSSE is evaluated along the scores defined in Sect. 4.2. The scores are given in % for the best correlation threshold for grouping the state space components as presented in Sect. 4.2. The influence score must be as close to 100 % as possible. The other two scores must be as small as possible. The regions are grouped along a correlation criterion r_{max} (see Sect. 4.2); we present the scores only for r_{max} with the best results. For OSSE 7, the scores are zeros for the fossil fuel regions because most of these regions were filtered out. The few remainings are very well constrained.

	OSSE 1		OSSE 2		OSSE 3		OSSE 4		OSSE 5		OSSE 6		OSSE 7	
Inversion inputs:														
x sub-totals	≠		=		=		≠		≠		=		≠	
x distributions	=		≠		=		≠		=		≠		≠	
H	=		=		≠		=		≠		≠		≠	
Optimal r_{max}	0.5		0.5		0.5		0.5		0.6		0.5		0.4	
Scores:	ff	wet	ff	wet	ff	wet	ff	wet	ff	wet	ff	wet	ff	wet
Relative score	79	94	16	27	40	84	3	66	30	117	20	93	0	112
Absolute score	9	16	2	11	36	24	1	27	18	40	37	30	0	15
Influence	63	56	39	37	45	30	37	28	46	58	32	32	13	33

Table 2. Eurasian site characteristics (Sect. 5.3). The altitudes of the sites are given as m a.s.l. and the inlet height is in m a.g.l.

| Station | ID | Location | | | Inlet |
		Lon ($^\circ$ E)	Lat ($^\circ$ N)	Alt (m a.s.l.)	height (m a.g.l.)
Azovo	AZV	73.03	54.71	100	50
Berezorechka	BRZ	84.33	56.15	150	80
Demyanskoe	DEM	70.87	59.79	75	63
Igrim	IGR	64.42	63.19	25	47
Karasevoe	KRS	82.42	58.25	50	67
Noyabrsk	NOY	75.78	63.43	100	43
Pallas	PAL	24.12	67.97	560	5
Shangdianzi	SDZ	117.12	40.65	287	0
Tae-ahn Peninsula	TAP	126.12	36.72	20	0
Ulaan Uul	UUM	11.08	44.45	914	0
Vaganovo	VGN	62.32	54.50	200	85
Yakutsk	YAK	129.36	62.09	210	77
Zotino	ZOT	89.35	60.80	104	301

Figure 1. Distribution of one component of the Monte-Carlo posterior ensemble. The histogram displays the raw posterior distribution. The dark hatched part of the histogram despicts the proportion of the ensemble within the tolerance interval TI_{68}, $[x^{low}, x^{high}]$ (as defined in Sect. 2.2). The red curve represents the Normal distribution with the same node and tolerance interval. The green curve stands for a Normal distribution with the same node and the same standard deviation.

Figure 2. Block diagram of the method. Green boxes represent the raw inputs of the system. The blue ones are intermediary results and red ones the outputs to be interpreted. The yellow ones depict the algorithms to compute. Details in Sects. 2 and 3. Insights for output analyses are given in Sect. 4.2.

Title Page

Abstract | Introduction

Conclusions | References

Tables | Figures

◄ | ►

◄ | ►

Back | Close

Full Screen / Esc

Printer-friendly Version

Interactive Discussion
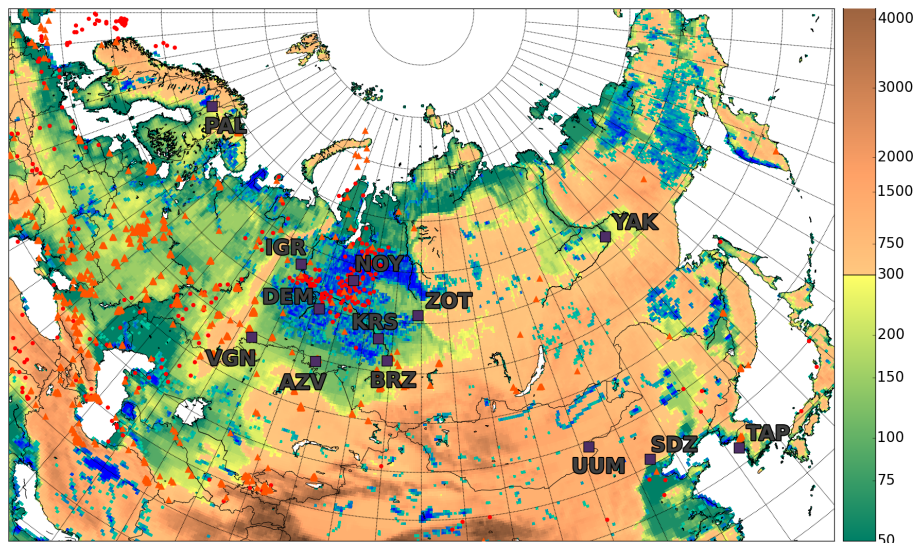
Figure 3. Topographic map of the domain of interest. The colorbar shows the altitude a.s.l. (from ETOPO1 database; Amante and Eakins, 2009). Red dots (resp. orange triangle) depicts hot spots of CH_4 emissions (based on EDGAR v4.2 inventory; see Sect. 5.1) related to oil welling and refineries (resp. gas extraction and leaks during distribution in population centers). Purple squares highlight the observation site localization. Blueish shaded areas represent average inundated regions, wetlands and peatlands (from the Global Lakes and Wetlands Database; Lehner and Döll, 2004).
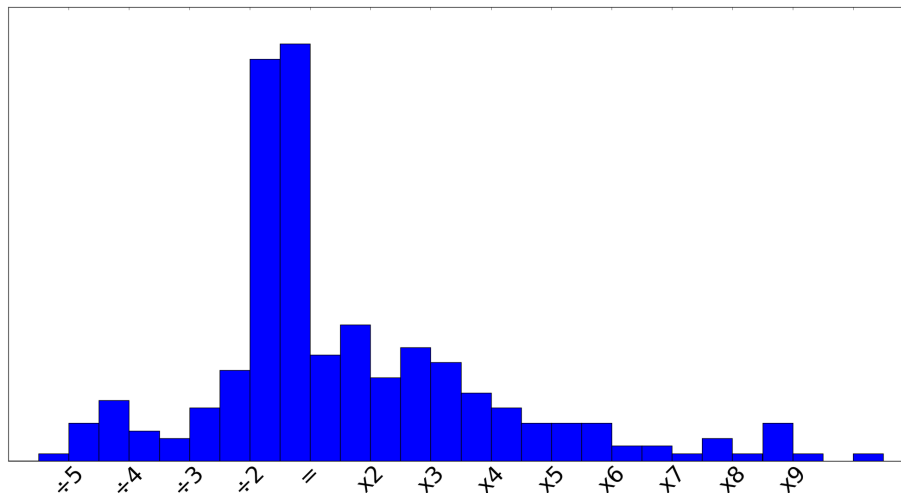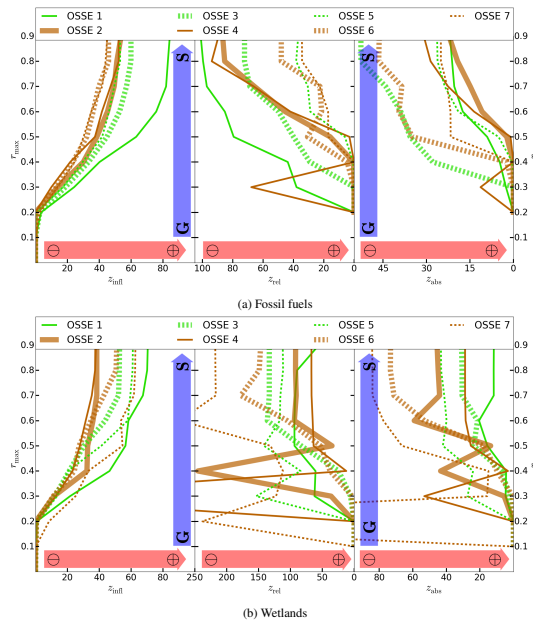
Figure 4. Distribution of the scaling factors applied to the emission databases in order to compute the "truth". All the emission component of the state vector have been included in the histogram. The selection of the scaling factor distribution is detailed in Sect. 5.1.

Objectified uncertainty quantification

A. Berchet et al.

(a) Fossil fuels

(b) Wetlands

Figure 5. Score comparison on fossil fuel (up) and wetland (bottom) regions for all OSSEs along correlation thresholds r_{max} of region grouping (see details in Sect. 4.2). (left) Influence correlation z_{infl} profile. (center) Relative score z_{rel} correlation profile. (right) Absolute score z_{abs} correlation profile. The red arrows depict the direction from lowest to best scores. The blue arrows denote the direction of grouping, from all grouped ("G", $r_{max} = 0$) to all separated ("S", $r_{max} = 1$). The OSSE are indexed along Table 1 numerotation. Thin (resp. thick) lines stand for correct (resp. perturbed) sub-total emissions. Green (resp. brown) lines depict correct (resp. perturbed) emission distributions. Plain (resp. dotted) lines represent correct (resp. perturbed) transport. As in Sect. 4.2, the scores are noted in %.
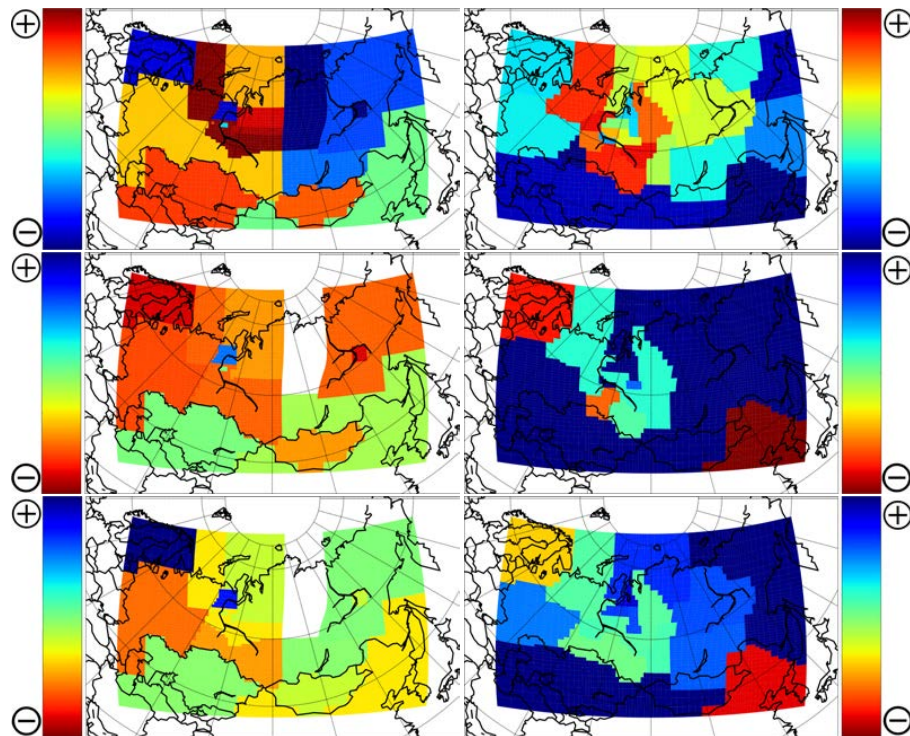
(a) Fossil fuels   (b) Wetlands

Figure 6. Map of the average scores as defined in Sect. 4.2 for the OSSE 1 (see Table 1) projected on the aggregation grid defined in Sect. 3. (up) Influence score z_{infl}. (middle) Relative score z_{rel}. (bottom) Absolute score z_{abs}. The color maps have been chosen so that the redder the region, the better its score (denoted by ⊖ and ⊕ symbols). The zoom and map physical projection are the same as in Fig. 3.

Full Screen / Esc

Printer-friendly Version

Interactive Discussion